

LITHOS

Parameterization of clinopyroxene growth kinetics via crystal size distribution (CSD) analysis: Insights into the temporal scales of magma dynamics at Mt. Etna volcano --Manuscript Draft--

Manuscript Number:	LITHOS9640
Article Type:	Regular Article
Keywords:	basalt; clinopyroxene; crystallization kinetics; crystal size distribution (CSD); magma cooling and decompression; Mt. Etna volcano
Abstract:	<p>There is increasing recognition that both textural and compositional changes of clinopyroxenes crystallizing from mafic alkaline magmas are the direct expression of complex dynamic processes extending over a broad range of spatial and temporal scales. Among others, supersaturation and relaxation phenomena play a key role in controlling the final crystal cargo of variably undercooled magmas erupted from active alkaline volcanoes. Following this line of reasoning, we have carried out isothermal-isobaric, decompression, and cooling rate experiments on a basalt interpreted as the parental magma of mafic alkaline eruptions at Mt. Etna volcano (Sicily, Italy). The main purpose is to reconstruct and quantify the textural changes (i.e., length of major and minor axes, surface area per unit volume, area fraction, and maximum growth rate) of clinopyroxene upon variable pressures (30-300 MPa), temperatures (1,050-1,100 °C), volatile contents (0-5 wt.% H₂O and 0-0.2 wt.% CO₂), and equilibration times (0.25-72 h). By integrating experimental data and thermodynamic modeling, the transition between interface-controlled (euhedral morphologies) and diffusion-controlled (anhedral morphologies) growth regimes has been determined at an undercooling threshold value of ~33 °C. Early melt supersaturation causes the fast growth of tiny clinopyroxenes with strong disequilibrium shapes, whereas an increasing relaxation time leads to the slow growth of large clinopyroxenes showing textural equilibration. According to these kinetic principles, both growth rate and relaxation time have been parameterized in relation to the crystal size distribution (CSD) analysis of naturally undercooled clinopyroxenes erupted during 2011-2012 lava fountain episodes at Mt. Etna volcano. Results indicate that the crystallization of microlites and microphenocrysts takes place under (dis)equilibrium growth conditions, in the order of ~10⁰⁻¹ min (large undercooling, short equilibration time) and ~10¹⁻² h (small undercooling, long equilibration time), respectively. This temporal information allows to disentangle the cooling and decompression paths of Etnean magmas rising and accelerating along a vertically extended, highly dynamic plumbing system. While clinopyroxene microlites develop during the fast ascent of magmas (~10⁰⁻¹ m s⁻¹) within the uppermost part of the conduit or immediately before ejection from the vent, the onset of microphenocryst crystallization occurs at depth and continues within the plumbing system during the slow ascent of magmas (~10⁻² m s⁻¹) that migrate through interconnected storage regions.</p>

**Parameterization of clinopyroxene growth kinetics via crystal size distribution (CSD) analysis:
Insights into the temporal scales of magma dynamics at Mt. Etna volcano**

^{1*}Piergiorgio Moschini, ^{1,2}Silvio Mollo, ¹Mario Gaeta, ³Sara Fanara, ²Manuela Nazzari, ⁴Chiara Maria
Petrone, ²Piergiorgio Scarlato

¹Department of Earth Sciences, Sapienza - University of Rome, P. le Aldo Moro 5, 00185 Roma, Italy

²Istituto Nazionale di Geofisica e Vulcanologia - Department Roma 1, Via di Vigna Murata 605, 00143
Roma, Italy

³Abteilung Experimentelle und Angewandte Mineralogie, Georg August Universität Göttingen,
Goldschmidtstraße 1, 37077 Göttingen, Germany

⁴The Natural History Museum, Department of Earth Sciences, Cromwell Road, SW7 5BD, London,
United Kingdom

*Corresponding author:

Piergiorgio Moschini

piergiorgio.moschini@uniroma1.it

Department of Earth Sciences

Sapienza - University of Rome

P. le Aldo Moro 5

00185 Roma, Italy

Abstract

There is increasing recognition that both textural and compositional changes of clinopyroxenes crystallizing from mafic alkaline magmas are the direct expression of complex dynamic processes extending over a broad range of spatial and temporal scales. Among others, supersaturation and relaxation phenomena play a key role in controlling the final crystal cargo of variably undercooled magmas erupted from active alkaline volcanoes. Following this line of reasoning, we have carried out isothermal-isobaric, decompression, and cooling rate experiments on a basalt interpreted as the parental magma of mafic alkaline eruptions at Mt. Etna volcano (Sicily, Italy). The main purpose is to reconstruct and quantify the textural changes (i.e., length of major and minor axes, surface area per unit volume, area fraction, and maximum growth rate) of clinopyroxene upon variable pressures (30-300 MPa), temperatures (1,050-1,100 °C), volatile contents (0-5 wt.% H₂O and 0-0.2 wt.% CO₂), and equilibration times (0.25-72 h). By integrating experimental data and thermodynamic modeling, the transition between interface-controlled (euhedral morphologies) and diffusion-controlled (anhedral morphologies) growth regimes has been determined at an undercooling threshold value of ~33 °C. Early melt supersaturation causes the fast growth of tiny clinopyroxenes with strong disequilibrium shapes, whereas an increasing relaxation time leads to the slow growth of large clinopyroxenes showing textural equilibration. According to these kinetic principles, both growth rate and relaxation time have been parameterized in relation to the crystal size distribution (CSD) analysis of naturally undercooled clinopyroxenes erupted during 2011-2012 lava fountain episodes at Mt. Etna volcano. Results indicate that the crystallization of microlites and microphenocrysts takes place under (dis)equilibrium growth conditions, in the order of ~10⁰-10¹ min (large undercooling, short equilibration time) and ~10¹-10² h (small undercooling, long equilibration time), respectively. This temporal information allows to disentangle the cooling and decompression paths of Etnean magmas rising and accelerating along a vertically extended, highly dynamic plumbing system. While clinopyroxene microlites develop during the fast ascent of magmas (~10⁰-10¹ m s⁻¹) within the uppermost part of the conduit or immediately before ejection from the vent, the onset of microphenocryst crystallization occurs at depth and continues within the plumbing system during the slow ascent of magmas (~10⁻² m s⁻¹) that migrate through interconnected storage regions.

Keywords: basalt; clinopyroxene; crystallization kinetics; crystal size distribution (CSD); magma cooling and decompression; magma ascent rate; Mt. Etna volcano.

Research Highlights

Clinopyroxenes from magmas erupted at Mt. Etna volcano have been investigated

Undercooling and relaxation time control the crystal growth rate and euhedrality

Time scales of magma dynamics are quantified by textural parameterization and CSD

Microlites record fast ascent of magmas along the uppermost part of the conduit

Microphenocrysts reflect slow growth within interconnected reservoirs at depth

1 **Parameterization of clinopyroxene growth kinetics via crystal size distribution (CSD) analysis:**
2 **Insights into the temporal scales of magma dynamics at Mt. Etna volcano**

3 ^{1*}Piergiorgio Moschini, ^{1,2}Silvio Mollo, ¹Mario Gaeta, ³Sara Fanara, ²Manuela Nazzari, ⁴Chiara Maria
4 Petrone, ²Piergiorgio Scarlato

5
6 ¹Department of Earth Sciences, Sapienza - University of Rome, P. le Aldo Moro 5, 00185 Roma, Italy

7 ²Istituto Nazionale di Geofisica e Vulcanologia - Department Roma 1, Via di Vigna Murata 605, 00143
8 Roma, Italy

9 ³Abteilung Experimentelle und Angewandte Mineralogie, Georg August Universität Göttingen,
10 Goldschmidtstraße 1, 37077 Göttingen, Germany

11 ⁴The Natural History Museum, Department of Earth Sciences, Cromwell Road, SW7 5BD, London,
12 United Kingdom

13
14 *Corresponding author:

15 Piergiorgio Moschini

16 piergiorgio.moschini@uniroma1.it

17 Department of Earth Sciences

18 Sapienza - University of Rome

19 P. le Aldo Moro 5

20 00185 Roma, Italy

21

22

23

24

25

26

27

28

29

30

31

32

33 **Abstract**

34 There is increasing recognition that both textural and compositional changes of clinopyroxenes
35 crystallizing from mafic alkaline magmas are the direct expression of complex dynamic processes
36 extending over a broad range of spatial and temporal scales. Among others, supersaturation and
37 relaxation phenomena play a key role in controlling the final crystal cargo of variably undercooled
38 magmas erupted from active alkaline volcanoes. Following this line of reasoning, we have carried out
39 isothermal-isobaric, decompression, and cooling rate experiments on a basalt interpreted as the parental
40 magma of mafic alkaline eruptions at Mt. Etna volcano (Sicily, Italy). The main purpose is to reconstruct
41 and quantify the textural changes (i.e., length of major and minor axes, surface area per unit volume, area
42 fraction, and maximum growth rate) of clinopyroxene upon variable pressures (30-300 MPa),
43 temperatures (1,050-1,100 °C), volatile contents (0-5 wt.% H₂O and 0-0.2 wt.% CO₂), and equilibration
44 times (0.25-72 h). By integrating experimental data and thermodynamic modeling, the transition between
45 interface-controlled (euhedral morphologies) and diffusion-controlled (anhedral morphologies) growth
46 regimes has been determined at an undercooling threshold value of ~33 °C. **Early melt supersaturation**
47 **causes the fast growth of tiny clinopyroxenes with strong disequilibrium shapes**, whereas an increasing
48 relaxation time leads to the slow growth of large clinopyroxenes showing textural equilibration.
49 **According to these kinetic principles, both growth rate and relaxation time have been parameterized in**
50 **relation to the crystal size distribution (CSD) analysis of naturally undercooled clinopyroxenes erupted**
51 **during 2011-2012 lava fountain episodes at Mt. Etna volcano**. Results indicate that the crystallization of
52 microlites and microphenocrysts takes place under **(dis)equilibrium** growth conditions, in the order of
53 ~10⁰-10¹ min (large undercooling, short equilibration time) and ~10¹-10² h (small undercooling, long
54 equilibration time), respectively. This temporal information allows to **disentangle the cooling and**
55 **decompression paths** of Etnean magmas rising and accelerating along a vertically extended, highly
56 dynamic plumbing system. While clinopyroxene microlites develop during the fast ascent of magmas
57 (~10⁰-10¹ m s⁻¹) within the uppermost part of the conduit or immediately before ejection from the vent,
58 the onset of microphenocryst crystallization occurs at depth and continues within the plumbing system
59 during the slow ascent of magmas (~10⁻² m s⁻¹) that migrate through interconnected storage regions.

60

61 **Keywords:** basalt; clinopyroxene; crystallization kinetics; crystal size distribution (CSD); magma
62 cooling and decompression; magma ascent rate; Mt. Etna volcano.

63

64

65 1. Introduction

66 Clinopyroxene is an important recorder of the physico-chemical changes explored by mafic
67 alkaline magmas typically occurring in intraplate settings. Owing to its ubiquitous crystallization over a
68 broad range of pressures, temperatures, and volatile contents (e.g., Mollo et al., 2018), a gamut of studies
69 have investigated the clinopyroxene textural and compositional variations in alkaline products, with the
70 main purpose of elucidating pre-eruptive magma storage conditions at depth and syn-eruptive dynamics
71 during ascent of magma towards the surface (e.g., Petrone et al., 2016, 2018; Ubide and Kamber, 2018).

72 While the stability field of clinopyroxene is intrinsically interrelated to the intensive and extensive
73 variables governing the thermodynamic reactions at the interface between crystal, melt, and fluid phases,
74 a certain degree of undercooling (ΔT) is essential to promote the growth and textural maturation of
75 clinopyroxene. ΔT is the thermodynamic driving force of crystallization and can be defined as the
76 difference between the temperature at which a specific mineral saturates the melt and the temperature of
77 a naturally solidifying system under variable cooling and degassing paths. Several reviews examined the
78 phenomenological aspects related to the kinetics of crystal nucleation and growth (e.g., Kirkpatrick,
79 1981; Cashman, 1990; Lasaga, 1998; Hammer, 2006; Mollo and Hammer, 2017; Giuliani et al., 2020),
80 along with increasing emphasis on the importance of magma supersaturation state to resolve specific
81 petrological and volcanological problems involving the environmental conditions of magmatic reservoirs
82 and their dynamic evolutions.

83 Recently, some authors (Hammer et al., 2016; Welsh et al., 2016; Ubide et al., 2019a, 2019b; Di
84 Stefano et al., 2020) focused their attention on the profound effect exercised by ΔT on the morphology
85 and composition of clinopyroxenes growing from mafic alkaline magmas, such as those erupted at
86 Haleakala (Hawaii) and Mt. Etna and Stromboli (Italy). These authors documented that systematic
87 departure from equilibrium arises by composite growth histories driven by imbalance between the rate
88 at which the crystal surface advance and the rate of cation diffusion in the melt. In particular, for magmas
89 erupted at Mt. Etna, it has been experimentally found that large ΔT causes strong supersaturation effects
90 leading to disequilibrium uptake of incompatible cations at the crystal-melt interface. These rate-limiting
91 concentration gradients promote preferential nucleation kinetics and fast development of small, anhedral
92 clinopyroxene crystals (Polacci et al., 2018; Arzilli et al., 2019; Masotta et al., 2020). Conversely, under
93 the driving force of small ΔT , the bulk system attempts to return to a near-equilibrium state between the
94 advancing crystal surface and the feeding melt composition. Because of the effect of enhanced growth
95 kinetics, large, euhedral clinopyroxenes develop by minimizing the interfacial free energy between
96 crystal and surrounding melt. Time-series experiments have also outlined that the shift from a diffusion-

97 controlled to an interface-controlled growth regime is intimately governed by relaxation phenomena
98 lowering the concentration gradients at the crystal-melt interface and leading to a steady-state textural
99 maturation of clinopyroxene (Pontesilli et al., 2019). After initial supersaturation effects, the growth rate
100 of clinopyroxene progressively decreases with increasing relaxation time, thereby approaching to a near-
101 equilibrium condition where attachment/detachment reactions of cations from the melt onto the
102 crystalline surface (and *vice versa*) occur at the same rate (Pontesilli et al., 2019). Some evidences from
103 time-series experiments corroborate also the textural maturation model proposed by Welsh et al. (2016)
104 for the growth of large clinopyroxene phenocrysts from basaltic magmas erupted at Haleakala. According
105 to the authors, the external morphology, chemical variation, and internal structure of these phenocrysts
106 testify to a continuous growth rate decrease over time, in response to less effective supersaturation
107 conditions driving gradual transition between diffusion-controlled and interface-controlled regimes
108 (Welsh et al., 2016).

109 Relying on previous laboratory data from Pontesilli et al. (2019) and Masotta et al. (2020), we
110 have conducted complementary isothermal-isobaric, decompression, and cooling rate experiments on a
111 primitive basalt from Mt. Etna, in order to unequivocally assess the control of supersaturation and
112 relaxation phenomena on clinopyroxene crystallization. In agreement with crystal growth
113 thermodynamics and kinetics, the textural maturation of clinopyroxene is attained at small undercoolings
114 and long equilibration times. Under such circumstances, we measure a growth rate decay of six orders
115 of magnitude that is modeled as a function of relaxation kinetics. This empirical relationship is
116 interpolated to the algebraic expression of crystal size distribution (CSD) analysis, with the final purpose
117 of quantifying the time scale of crystallization during cooling and decompression of mafic alkaline
118 magmas. As a test case, microlites and microphenocrysts from scoria clasts ejected during 2011-2012
119 lava fountains at Mt. Etna have been considered. Results from calculations give rise to a conceptual
120 model for the time scale of magma dynamics recorded by the (dis)equilibrium textural evolution of
121 clinopyroxene and for the rapid acceleration of magma ascending within the volcanic conduit,
122 immediately before eruption at the vent.

123

124 2. Methods

125 2.1. Experimental strategy

126 The starting material used for the experiments is a natural basalt from the Monte Maletto
127 Formation erupted at Mt. Etna around 7,000 years ago. Monte Maletto Formation comprises basaltic to
128 trachybasaltic products that have been interpreted by numerous authors as the parental compositions of

129 **historic and recent Etnean eruptions** (see the review study of [Mollo et al., 2018](#) and references therein).
130 The powdered rock was melted to ensure homogeneity of the final starting material at the HP-HT
131 Laboratory of Experimental Volcanology and Geophysics of the Istituto Nazionale di Geofisica e
132 Vulcanologia (INGV), Rome, Italy. A crucible containing the natural powder was loaded in a 1 atm
133 vertical tube CO–CO₂ gas-mixing furnace at 1,300 °C for 1 h. The redox state was **1 log unit above the**
134 **Ni-NiO buffer (NNO+2)**, comparable to that estimated at the Mt. Etna ([Mollo et al., 2015a](#)). Iron loss
135 was kept to < 5% of the initial amount by adopting **a Fe pre-saturated Pt crucible**. The quenched glass
136 was analyzed by scanning electron microscopy and no crystalline phases were detected. Twenty
137 microprobe analyses of the glass yielded an average composition (in wt.%) of 47.56 (±0.39) SiO₂, 1.48
138 (±0.11) TiO₂, 15.42 (±0.23) Al₂O₃, 10.79 (±0.17) FeO_{tot}, 0.21 (±0.04) MnO, 7.98 (±0.15) MgO, 12.13
139 (±0.18) CaO, 2.61 (±0.13) Na₂O, 1.25 (±0.12) K₂O, and 0.57 (±0.04) P₂O₅.

140 Isothermal and decompression experiments were carried out in an internally heated pressure
141 vessel (IHPV) equipped with a continuum decompression system and a rapid quenching device (drop
142 quench) at the Abteilung Experimentelle und Angewandte Mineralogie, Georg August Universität
143 Göttingen (Germany). The powdered starting glass was loaded in **Fe-presaturated Pt-capsules**. Isobaric
144 experiments (*Experimental Set ISO*) **were conducted at 300 MPa and temperatures of 1,100 (ISO-1100),**
145 **1,075 (ISO-1075), and 1,050 °C (ISO-1050)** that were kept constant over an equilibration time of ~24
146 hours ([Table 1](#)). The experiments were designed under nominally anhydrous and hydrous conditions,
147 corresponding to 0 wt.% H₂O_{initial} (*ISO-0H2O*, i.e., nominally anhydrous system), 2 wt.% H₂O_{initial} (*ISO-*
148 *2H2O*), 5 wt.% H₂O_{initial} (*ISO-5H2O*), and 2 wt.% H₂O_{initial} + 0.2 wt.% CO_{2initial} (*ISO-H2O+CO2*). H₂O
149 and CO₂ were added as deionized water and oxalic acid, respectively. Decompression experiments
150 (*Experimental Set ΔP*) were conducted at the **same temperatures** and anhydrous-hydrous conditions by
151 depressurizing the charges from 300 to 30 MPa at slow (*ΔPs*) and fast (*ΔPf*) rates of 0.018 and 0.98 MPa
152 s⁻¹, respectively ([Table 1](#)). Pressures, temperatures, and melt-H₂O+CO₂ contents have been selected in
153 order to reproduce the most common crystallization-degassing path of magmas at Mt. Etna, as derived
154 by thermobarometric-hygrometric calculations and melt inclusion data ([Mollo et al., 2018 and references](#)
155 [therein](#)). Slow to fast decompression experiments correspond to magma ascent velocities in the range of
156 0.45-24.5 m s⁻¹, in agreement with previous estimates suggested by geophysical, crystallochemical, and
157 numerical studies focusing on magma conduit dynamics ([Aloisi et al., 2006; Mollo et al., 2015b; La](#)
158 [Spina et al., 2016; Giuffrida et al., 2017](#)). Note that, the **solubility** of H₂O in this melt composition is ~2.9
159 and ~0.5 wt.% at 300 (i.e., fluid-absent) and 30 (i.e., fluid-present) MPa, respectively, as derived by the
160 thermodynamic model of [Duan \(2014\)](#) and corroborated by numerous studies carried out on mafic

161 alkaline magmas (Mollo et al., 2018 and references therein). Coherently, magma dynamics at Mt. Etna
162 volcano are frequently recognized as the result of complex crystallization regimes that, at shallow crustal
163 levels, ~~unexpectedly~~ change from H₂O-undersaturated to H₂O-saturated (i.e., $P_{H_2O} = P_{total}$) conditions, in
164 conjunction with abundant volatile degassing (Mollo et al., 2015b, 2018; Perinelli et al., 2016, 2018).
165 The temperature was monitored by three S-type (Pt90Rh10/Pt) thermocouples and pressure was recorded
166 by a transducer, calibrated against a Heise tube gauge with accuracy ± 5 MPa. Experiments were
167 quenched using a drop quench device imposing a cooling rate of ~ 150 °C s⁻¹. Recovered charges were
168 mounted in epoxy and polished thin sections was produced from the epoxy blocks. The use of Ar as a
169 pressure medium provided an intrinsic fO_2 variable from NNO+2 to NNO+4 (Schanofski et al., 2019).
170 Within the sample capsule, fH_2 was controlled by hydrogen permeation through the capsule walls driven
171 by the fugacity gradient between the pressure medium and the capsule interior. This in turn determined
172 the fO_2 inside the capsule through the equilibrium $H_2 + 1/2 O_2 \leftrightarrow H_2O$. However, under fluid-present
173 conditions and with the addition of CO₂, the redox state of the system changed in response to the variable
174 activity of H₂O in the melt (Botcharnikov et al. 2008). In this respect, the redox state of the system was
175 estimated at the end of experimental runs through the oxygen barometer of Ishibashi (2013) based on
176 spinel–melt equilibria and with uncertainty (± 0.3 log unit). This model was calibrated using a alkaline
177 data set, returning fO_2 estimates variable from NNO+1.9 and NNO+2.3 buffer (Mollo et al., 2015a).

178 Cooling rate experiments (Table 1) were carried out in a non-end loaded piston cylinder apparatus
179 (“QUICKpress”, Depths of the Earth co.) using a 19-mm NaCl-pyrex-graphite-MgO assembly that
180 produced a redox state close to NNO+2 buffer (Mollo and Masotta, 2014). The assembly was loaded
181 with a Fe-presaturated Pt-capsule containing the hydrous (2 wt.% H₂O_{initial}) glass. The capsules were
182 surrounded by powdered pyrophyllite to prevent H₂O loss and enhance stress homogenization during
183 initial compression. After cold pressurization to a nominal pressure 10% higher than desired, the pressure
184 was decreased down to 300 MPa. The temperature was monitored by a factory-calibrated C-type (W-
185 5Re/W-26Re) thermocouple. Following Masotta et al. (2020), the experiments were carried out by
186 heating the starting glass to superliquidus condition of 1,300 °C at a rate of 80 °C min⁻¹. After 30 min,
187 the temperature was cooled to 1,050 °C at the same rate of 80 °C min⁻¹ (Experimental Set CR). This
188 isothermal condition was kept constant for 0.25 (CR-025), 0.5 (CR-05), 1 (CR-1), 4 (CR-4), 24 (CR-24),
189 and 72 (CR-72) hours, before isobaric quench at a rate of 100 °C s⁻¹ (Table 1).

190

191 2.2. Image processing and CSD correction

192 Photomicrographs of the experimental products were collected in backscattered electron (BSE)
193 mode of a JEOL 6500F field emission gun scanning electron microscopy (FE-SEM) equipped with an
194 energy-dispersive spectrometer (EDS) detector at the HP-HT Lab of INGV.

195 The acquired photomicrographs were processed via NIH Image J software and reduced to binary
196 type images (i.e., black and white color) by grey level thresholding (i.e., image segmentation; [Armienti,
197 2008](#)). The segmentation method was employed to identify clinopyroxene microphenocrysts and
198 microlites relative to other mineral phases ([Fig. 1](#)). A Matlab© code (see [Supplementary Material 1](#)) was
199 developed to perform image processing operations in conjunction with NIH Image J. The retrieved
200 textural parameters were 1) the equal-area best-fit ellipses and lengths of major (L) and minor (W) axes
201 ([Fig. 1](#)), 2) the surface area per unit volume (S_v^P as 3D aspect ratio; [Table 1](#)), and 3) the area fraction of
202 a given population within a plane that is comparable to its volume fraction (ϕ). Following one of the
203 most common methods reported in literature (cf. [Pontesilli et al., 2019 and references therein](#)), L and W
204 data were used to calculate the maximum growth rate (G_{max} in mm s^{-1}) of clinopyroxene, as an average
205 of the ten largest crystals measured in each experimental run ([Supplementary Material 2](#)):

$$206$$
$$207 \quad G_{max} = (L W)^{0.5} / (2 t) \quad (1)$$
$$208$$

209 where t is the experimental time.

210 The magnitude of S_v^P was determined as ([Hammer, 2006](#)):

$$211$$
$$212 \quad S_v^P = S_v^T / \phi \quad (2)$$
$$213$$

214 S_v^T is the total interfacial area of a population per unit volume of sample and can be expressed as $2 \times N_L$,
215 where N_L is the density of phase boundary intersections in a given length of randomly oriented test line.
216 The Matlab© code from this study allows to overlay the desired number of circular test lines over a
217 binary type image ([Fig. 1](#)) and determine the N_L value by counting the locus of points where crystal-melt
218 boundaries intersect the test lines. The lower is the magnitude of S_v^P parameter, the higher is the crystal
219 euhedrality. Therefore, clinopyroxenes characterized by $S_v^P < 1,000 \text{ mm}^{-1}$ are interpreted as euhedral,
220 whereas crystal with $S_v^P > 1,000 \text{ mm}^{-1}$ are anhedral ([Hammer, 2008](#)). S_v^P data listed in [Table 1](#) are the
221 mean resulting from the analysis of eight binary type images for sample, each one overlaid by six circles
222 with radius variable as a function of BSE image magnification ([Fig. 1](#)).

223 CSD analysis was carried out on BSE images of natural rock samples from 2011-2012 lava
 224 fountains outpoured at Mt. Etna volcano. Textural data were collected at $\times 500$ and $\times 100$ magnifications
 225 for microlites (< 0.1 mm) and microphenocrysts (≥ 0.1 mm) populations, respectively, and then combined
 226 each other to obtain one single CSD curve. Intersection planar data were converted in volume data by
 227 applying **stereological correction**, in order to gain information on the contribution of larger crystals to
 228 the population of smaller ones. This correction method accounts for 1) potential cut-section effects in
 229 case of larger crystals are cut by a plane shifted with respect to the center, therefore contributing to
 230 smaller crystal populations, and 2) intersection probability effects when, for a poly-disperse distribution,
 231 smaller crystals are less likely to be intersected by a plane than larger crystals (Higgins, 2000). The
 232 crystal shape, assumed as the crystal aspect ratio S:I:L of short:intermediate:long dimensions (Higgins,
 233 2000), was determined by the Excel© spreadsheet *CSDslice* developed by Morgan and Jerram (2006).
 234 Through this model, 2D raw data were compared with a crystal habit database (i.e., S:I:L of 1:10:10,
 235 1:1:10, and 1:1:1) to constrain the five best-matching crystal shapes. The best linear binning was selected
 236 for each sample by the procedure reported in Armienti (2008) for the minimization of residuals between
 237 the particles effectively measured and those re-calculated by CSD analysis (zeroth moment of the
 238 distribution):

$$240 \quad N_{tot} = Area \sum L_i N_V(L_i) \quad (3)$$

241
 242 where L_D , N_A , and N_V (i.e., the ratio of N_A to L_D) are the characteristic crystal size, the area number density
 243 and volumetric number density, respectively. The routine of Armienti (2008) requires also the
 244 minimization of residuals between the measured volume crystal fraction and the volume resulting from
 245 CSD analysis (third moment of the distribution):

$$247 \quad V_f = \sum N_V(L_i) \frac{4}{3} \pi \left(\frac{L_i}{2}\right)^3 = \frac{\pi}{6} \sum L_i^3 N_V(L_i) \quad (4)$$

248
 249 According to Eqns. (3) and (4), a linear binning ΔL of 0.02 mm was derived, for a total of 21 classes
 250 ranging from 0.006 to 0.406 mm. Crystals with $L < 0.006$ mm (i.e., artefacts caused by image
 251 segmentation) and crystal fragments at the edge of photomicrographs were removed from the dataset
 252 (Armienti et al., 1994). The program *CSDCorrections* 1.38 of Higgins (2000) was finally employed to
 253 calculate a binned CSD curve for different crystal size classes by specifying the crystal shape values

254 reported in [Supplementary Material 3](#), rock fabric of massive type, and crystal roundness factor of 0.5.
255 The formulated CSD diagrams are in the form of semi-logarithmic plots based on $\ln N(L)$ vs. L that
256 describe the evolution of crystal size as ([Marsh, 1988](#)):

$$258 \ln N(L) = \frac{-L}{G \tau} + \ln N_0 \quad (5)$$

259
260 where $N(L)$ is the number of crystals per size of length L per unit volume (i.e., the density distribution of
261 crystals per unit volume per bin size), G is the crystal growth rate, τ is the time of a system crystallizing
262 at steady state, and N_0 is the nucleation density (i.e., the number of crystals of **zero size**). When the
263 dominant size of the crystal population results from **steady growth over an appropriate duration of time**,
264 the linear regression fit of CSD curve has slope $m = 1 / (G \times \tau)$ and intercept $b = \ln(N_0)$. CSD statistics
265 were obtained from the quantitative study of 16 thin sections and 243 photomicrographs. CSD plots were
266 constructed considering ~1,500-4,000 crystals.

268 2.3. Microanalysis

269 Major element concentrations were obtained at the HP-HT Lab of INGV using a JEOL-JXA8200
270 electron probe micro-analyzer (EPMA) equipped with five ~~wave~~ dispersive spectrometers
271 ([Supplementary Material 4](#)). For glasses, a slightly defocused 3 μm beam was used with a counting time
272 of 5 s on background and 15 s on peak. For crystals, beam size was 1 μm with a counting time of 20 and
273 10 s on peak and background, respectively. The following standards were used for calibration: jadeite
274 (Si and Na), corundum (Al), forsterite (Mg), andradite (Fe), rutile (Ti), orthoclase (K), barite (Ba), apatite
275 (P), spessartine (Mn) and chromite (Cr). Sodium and potassium were analyzed first to prevent alkali
276 migration effects. The precision of the microprobe was measured through the analysis of **well-**
277 **characterized synthetic standards**. Based on counting statistics, analytical uncertainties relative to their
278 reported concentrations indicate that precision and accuracy were better than 5% for all cations.

280 3. Results

281 3.1. Textural features

282 Selected BSE photomicrographs representative of run products from *Experimental Set ISO*,

283 *Experimental Set ΔP*, and *Experimental Set CR* are displayed in [Figs. 1](#) and [2](#) (note that photomicrographs
284 of all the experiments are reported in [Supplementary Material 2](#)). The mineral assemblage consists of
285 abundant clinopyroxene and titanomagnetite, with subordinate plagioclase.

286 Clinopyroxenes from *Experimental Set ISO* show euhedral morphologies, with a great number of
287 well-faced crystals ([Figs. 1](#) and [2](#)) and L_{max} variable from 0.07 to 0.23 mm ([Supplementary Material 2](#)).
288 Run products are characterized by a dense mosaic of either isolated or aggregated microlites, suggesting
289 rapid attainment of an interface-controlled crystal growth regime. Indeed, most of clinopyroxene
290 crystallization initiated upon crossing the glass transition temperature ($T_g = 723$ °C, [Giordano et al.,](#)
291 [2005](#)) and further continued over time (i.e., there is no effective ΔT caused by cooling and/or
292 decompression). The amount of residual glass found in the experimental charges increases with
293 increasing T and $H_2O_{initial}$ ([Figs. 1](#) and [2](#), and [Supplementary Material 2](#)). In contrast, the presence of CO_2
294 lowers the amount of H_2O dissolved in the melt, raising the liquidus temperature of the experimental
295 system and increasing the crystal content ([Supplementary Material 2](#)).

296 Clinopyroxenes from *Experimental Set ΔP* consist of sector-zoned crystals with prismatic shapes
297 and well-formed planar edges ([Figs. 1](#) and [2](#), and [Supplementary Material 2](#)). L_{max} ranges from 0.02 to
298 0.25 mm, depicting an increasing trend with increasing T and $H_2O_{initial}$. Under slow decompression
299 regimes, the crystal size substantially increases due to the effect of sluggish decompression-driven crystal
300 growth kinetics. Therefore, L_{max} measured for $\Delta P_s-1100-5H_2O$ (0.14-0.25 mm) is much higher than that
301 determined for $\Delta P_f-1100-5H_2O$ (0.06-0.09 mm). Notably, the lack of anhedral (hopper to dendritic)
302 forms in both ΔP_s and ΔP_f experiments accounts for the effect of relative slow ΔT (14-30 °C; [Table 1](#)),
303 consistently with previous literature data (see the review study of [Giuliani et al., 2020](#)).

304 Clinopyroxenes from *Experimental Set CR* show substantial textural differences as a function of
305 relaxation time ([Figs. 1](#) and [2](#), and [Supplementary Material 2](#)). *CR-1050-025*, *CR-1050-05*, and *CR-1050-*
306 *1* are characterized by the ubiquitous occurrence of acicular and skeletal crystals, whereas *CR-1050-4*,
307 *CR-1050-24*, and *CR-1050-72* exhibit clear euhedral morphologies ([Fig. 2](#) and [Supplementary Material](#)
308 [2](#)). The shift from a diffusion-controlled to an interface-controlled crystal growth conditions is marked,
309 taking place in a time interval comprised between 1 and 4 h. Once crystallization proceeds under
310 nucleation-dominated regimes, L_{max} ranges from 0.07 to 0.10 mm for *CR-1050-025*, *CR-1050-05*, and
311 *CR-1050-1*. In contrast, due to superimposition of growth-dominated regimes, L_{max} ranges from 0.08 to
312 0.25 mm for *CR-1050-4*, *CR-1050-24*, and *CR-1050-72*.

313

314 3.2. Crystal content variation

315 Fig. 3 shows the variation of clinopyroxene content (% area) in *Experimental Set ISO*,
316 *Experimental Set ΔP*, and *Experimental Set CR*.

317 As the target temperature increases, the degree of crystallization decreases from 28% to 18% and
318 from 21% to 5% for *Experimental Set ISO* and *Experimental Set ΔP*, respectively (Fig. 3a). A similar
319 decrease is attained by increasing H_2O_{initial} , whereas the crystal content slightly increases by ~4% when
320 CO_2 is added to the experimental charge.

321 *Experimental Set CR* exhibits the highest clinopyroxene content within the whole data set. As the
322 relaxation time increases, the degree of crystallization slightly decreases from 37% to 32% (Fig. 3b). A
323 modest drop in crystal content takes place in the time interval comprised between 1 and 4 h, once the
324 crystallization regime shifts from nucleation-dominated to growth-dominated regimes.

325

326 3.3. Clinopyroxene euhedrality

327 Fig. 4 shows the variation of S_v^P determined for *Experimental Set ISO*, *Experimental Set ΔP*, and
328 *Experimental Set CR*. The effect of temperature and H_2O_{initial} on S_v^P is that to decrease the surface area of
329 clinopyroxene per unit volume. An increasing number of crystals enhances the probability of phase
330 boundary intersections and, consequently, most of trends defined for S_v^P are comparable to those derived
331 for the clinopyroxene content (compare Figs. 3 and 4).

332 For *Experimental Set ISO* ($730\text{-}477\text{ mm}^{-1} S_v^P$) and *Experimental Set ΔP* ($548\text{-}113\text{ mm}^{-1} S_v^P$), the
333 euhedrality of clinopyroxene increases with increasing temperature and H_2O_{initial} (Fig. 4a). Both
334 isothermal and decompression data confirm that values of $S_v^P < 1,000\text{ mm}^{-1}$ account for the development
335 of well-faced morphologies (cf. Hammer, 2008).

336 On the other hand, the magnitude of crystal euhedrality radically changes in *Experimental Set CR*
337 (Fig. 4b). S_v^P ranges from 1,365 to 1,194 mm^{-1} for *CR-1050-025*, *CR-1050-05* and *CR-1050-1*. A much
338 more restricted S_v^P range of 896-815 mm^{-1} is measured for *CR-1050-4*, *CR-1050-24*, and *CR-1050-72*.
339 Since the experimental cooling rate was fixed and only the relaxation time was changed, the abrupt
340 variation of S_v^P is a proxy for the control of relaxation time on the crystallization regime, after that the
341 system is subjected to an early stage of undercooling (Arzilli et al., 2018; Pontesilli et al., 2019).

342

343 3.4. Compositional features

344 Chemical changes of residual glasses and coexisting clinopyroxene crystals will be the object of
345 a forthcoming and more comprehensive work on cation partitioning under isobaric-isothermal vs.

346 cooling-decompression conditions. Here we briefly summarize the most important compositional
347 features of the experimental charges (Fig. 5):

348 1) according to the TAS (total alkali vs. silica) classification diagram, the glass chemistry (Fig. 5a) can
349 be divided into two groups as a function of temperature and $H_2O_{initial}$ conditions (i.e., the degree of
350 crystallization);

351 2) at high- T (1,100 °C), high- $H_2O_{initial}$ contents (5 wt.%), residual melts exhibit basaltic-trachybasaltic
352 compositions (Fig. 5a) similar to those of recent (post-1971) eruptions at Mt. Etna volcano (natural data
353 set from Mollo et al., 2018);

354 3) at low- T (1,050-1,075 °C), low- $H_2O_{initial}$ contents (0-2 wt.%), residual melts are more differentiated,
355 resembling trachybasalts to basaltic trachyandesites erupted during the historic (pre-1971) period of
356 activity (Fig. 5a);

357 4) clinopyroxene chemistry follows the same evolutionary path depicted by the melt phase, with the
358 exception of sector-zoned crystals obtained under slow and fast decompression conditions (Fig. 5b);

359 5) at high- T , high- $H_2O_{initial}$ contents, clinopyroxenes are enriched in Di (diopside) + Hd (hedenbergite)
360 and depleted in CaTs (Ca-Tschermak) + CaTiTs (CaTi-Tschermak) components (Fig. 5b);

361 6) at low- T , low- $H_2O_{initial}$ contents, the amount of Di + Hd in clinopyroxenes decreases at the expense
362 of CaTs + CaTiTs (Fig. 5b), responding to the higher degree of melt differentiation;

363 7) kinetic effects in decompression experiments produce sector-zoned clinopyroxenes characterized by
364 Di-Hd-rich, CaTs-CaTiTs-poor hourglass (or basal) sectors $\{-1\ 1\ 1\}$ and Di-Hd-poor, CaTs-CaTiTs-rich
365 prism sectors $\{1\ 0\ 0\}$;

366 8) the chemistry of hourglass sectors $\{-1\ 1\ 1\}$ closely matches with that of experimental crystals obtained
367 at high- T , high- $H_2O_{initial}$ contents, as well as with the natural hourglass sectors of phenocrysts from recent
368 eruptions at Mt. Etna volcano;

369 9) the chemistry of prism sectors $\{1\ 0\ 0\}$ depicts a distinct crystal population, with substantial enrichment
370 in Tschermak components, as also observed for the prism sectors of clinopyroxene phenocrysts from
371 recent eruptions;

372 10) overall, the development of sector-zoned clinopyroxenes from decompression experiments is
373 consistent with kinetic cation partitioning caused by decompression and degassing of Etnean magmas
374 (Ubide and Kamber, 2018; Masotta et al., 2020), in conjunction with charge balance mechanisms due to
375 $Si^{4+} \leftrightarrow Al^{3+}$ substitution in the tetrahedral site and $Mg^{2+} + Fe^{2+} \leftrightarrow Ti^{4+} + Fe^{3+}$ exchange in octahedral
376 sites (Mollo et al., 2018).

377

378 4. Discussion

379 4.1. Clinopyroxene growth rate and thermodynamic constraints

380 Values of G_{max} for clinopyroxenes from this study are listed in Table 1 and plotted in Fig. 6 on a
381 logarithmic scale as a function of the different experimental conditions.

382 For *Experimental Set ISO* and *Experimental Set ΔP* , the value of G_{max} is positively correlated with
383 temperature and $H_2O_{initial}$, but this correlation is much more evident for the decompression experiments
384 rather than isothermal runs (Fig. 6a). Major changes of G_{max} are measured as the experimental conditions
385 change in the order of *Experimental Set ISO* ($\sim 10^{-15}$ - 10^{-14} mm s⁻¹), *Experimental Set ΔP_s* ($\sim 10^{-14}$ - 10^{-12}
386 mm s⁻¹), and *Experimental Set ΔP_f* ($\sim 10^{-10}$ - 10^{-9} mm s⁻¹).

387 On one hand, under isothermal conditions, the early nucleation of clinopyroxene takes place when
388 the system is heated directly to the target temperature. As a consequence, any effect related to melt
389 supersaturation is mitigated by the absence of true degree of ΔT , resulting from a time-temperature path
390 experienced by the melt and controlling the kinetic growth of clinopyroxene (Baker, 2008). Hence, the
391 bulk system tends to minimize the interfacial free energy between small size crystals and the surrounding
392 melt (Bonechi et al., 2020; Masotta et al., 2020), resulting in a closer approach to equilibrium far from
393 dynamic undercooling conditions encountered by magmas rising along the shallower parts of a plumbing
394 system and/or along the volcanic conduit (Mollo and Hammer, 2017 and references therein). Therefore,
395 the rate of attachment/detachment reactions of cations from the melt onto the crystalline surface (and
396 *vice versa*) attains to a steady-state condition in a relatively short experimental time (Kirkpatrick, 1981,
397 1983; Pontesilli et al., 2019).

398 On the other hand, the control of ΔT (14-30 °C) on G_{max} is more effective under decompression
399 conditions (Fig. 6a). H_2O exsolution, as a result of decompression, raises the liquidus region of the melt,
400 thus imposing a certain degree of melt supersaturation and facilitating the growth of clinopyroxene
401 (Simakin et al., 2003; Orlando et al., 2008; Hammer, 2008; Mollo and Hammer, 2017). Moreover, Fig.
402 6a shows that the magnitude of G_{max} from H_2O - CO_2 -bearing charges ($\Delta T = 14$ - 18 °C) is systematically
403 lower than that measured for H_2O -bearing charges ($\Delta T = 16$ - 30 °C), accounting for the presence of CO_2
404 and its rival effect on H_2O contents dissolved in the melt. This observation is consistent with the
405 knowledge that a slow mobility of Si and Al in low- T , low- H_2O melts is rate-limiting for divalent Ca and
406 Mg cations, and the addition of tetrahedral groups to the surface of a crystal is the rate-controlling step
407 of the crystal growth (Nascimento et al., 2004).

408 For *Experimental Set CR*, the effect of ΔT (125 °C) on G_{max} is exacerbated by strong melt
 409 supersaturation phenomena and the crystal growth regime shifts from interface-controlled to diffusion-
 410 controlled (Lofgren, 1974; Sunagawa, 1981; Webb and Dingwell, 1995). Nonetheless, as reported in
 411 Pontesilli et al. (2019), the role played by relaxation kinetics on the crystal growth becomes increasingly
 412 more effective with time. G_{max} decreases by orders of magnitude, from $\sim 10^{-11}$ (CR-1050-025) to $\sim 10^{-15}$
 413 mm s⁻¹ (CR-1050-72) (Fig. 6b). Short relaxation times of 0.25-1 h favor melt supersaturation and
 414 diffusion-limited growth regimes, with more pronounced nucleation of crystals showing disequilibrium
 415 textures (Mollo et al., 2010, 2012; Lofgren, 1974; Sunagawa, 1981). As the relaxation time increases up
 416 to 72 h, an interface-controlled growth promotes formation of euhedral crystals (Fig. 6b). This textural
 417 maturation pairs with the progressive decay of G_{max} towards a steady-state condition (Hammer, 2006,
 418 2008; Pontesilli et al., 2019).

419 The dependence of crystal growth rate on the degree undercooling can be explicitly defined as
 420 (Cashman 1990; Toramaru 1991; Armienti, 2008):

421

$$422 \quad G \propto \exp\left(\frac{-E}{RT_{exp}}\right) \left[1 - \exp\left(\frac{-\Delta H \Delta T}{k T_{exp} T_{liquidus}}\right)\right] \quad (6)$$

423

424 where R and k are the gas ($8.310 \text{ J mol}^{-1} \text{ K}^{-1}$) and Boltzmann ($1.382 \times 10^{-23} \text{ J K}^{-1}$) constants, respectively.
 425 ΔH is the molar enthalpy of fusion ($50\text{-}100 \text{ kJ mol}^{-1}$; Weill et al., 1980; Toramaru, 1991) and E is the
 426 activation energy of clinopyroxene crystal growth ($200\text{-}377 \text{ kJ mol}^{-1}$; Toramaru, 1991; Yilmaz et al.,
 427 1996; Karamarov et al., 2000; Burkhard, 2005). T_{exp} is the experimental temperature, whereas $T_{liquidus}$ is
 428 the liquidus temperature of 1,150-1,220 °C, as determined by rhyolite-MELTS thermodynamic
 429 simulations carried out at 300 MPa, 0-5 wt.% H₂O, and NNO+2 buffer (v.1.2.0; Gualda et al., 2012).
 430 Within these thermodynamic constraints, the growth rates estimated for clinopyroxene are $\sim 10^{-11}\text{-}10^{-9}$
 431 mm s⁻¹ (*Experimental Set ΔP_f*), $\sim 10^{-13}\text{-}10^{-12}$ mm s⁻¹ (*Experimental Set ΔP_s*), and $\sim 10^{-15}\text{-}10^{-14}$ mm s⁻¹
 432 (*Experimental Set CR*). Fig. 6a shows that G_{max} values modeled for *Experimental Set ΔP* are comparable
 433 with those measured in laboratory, also corroborating the strong control of ΔT on clinopyroxene
 434 crystallization. However, for *Experimental Set CR*, the derived thermodynamic quantities match only
 435 with G_{max} measured for CR-1050-24 and CR-1050-72 experiments (Fig. 6b), whereas Eqn. (6) fails to
 436 predict G_{max} at shorter relaxation times of 0.25, 0.5, 1, and 4 h. From a comparatively textural analysis
 437 emerges that crystal growth mismatches are caused by strong nucleation kinetics and abundant dendritic
 438 crystallization (Fig. 2). A higher nucleation rate over a shorter relaxation time causes a more pronounced

439 melt supersaturation and a diffusion-controlled growth regime (Toramaru, 1991). This agrees 4D
 440 crystallization experiments conducted by Arzilli et al. (2019) on a trachybasalt erupted during 2001
 441 eruption at Mt. Etna. At $\Delta T \geq 60$ °C and dwell time of 4 h, dendritic clinopyroxene crystals develop by
 442 diffusion-controlled branching growth in multiple directions to reach a maximum size of 40 μm (Arzilli
 443 et al., 2019). In contrast, as the relaxation time increases, early dendritic crystals are replaced by euhedral
 444 morphologies typical of interface-controlled growth regimes (Fig. 2). Under such circumstances, the
 445 attachment of cations on the crystal surface is enhanced by a decrease of melt supersaturation
 446 (Kirkpatrick, 1981, 1983) which, in turn, is more adequately modeled by Eqn. (6) for CR-1050-24 and
 447 CR-1050-72 experiments (Fig. 6b).

448 According to clinopyroxene growth kinetics, the transition between interface-controlled and
 449 diffusion-controlled regimes is governed by a screw dislocation growth model, where the crystal-melt
 450 interface is assumed to be smooth and growth takes place at step sites provided by screw dislocations
 451 (Kirkpatrick et al., 1981, 1983). The thermodynamic equations behind screw dislocations are
 452 approximated to a temperature-dependent growth rate system (Nascimento et al., 2004):

453
 454
$$G = f \frac{D}{\lambda} \left[1 - \exp\left(-\frac{|\Delta G|}{RT}\right) \right], \quad (7)$$

455
 456
$$f = \frac{\lambda \Delta G}{4 \pi \sigma V}, \text{ and} \quad (8)$$

457
 458
$$\sigma = \frac{\alpha \Delta H \lambda}{V} \quad (9)$$

459
 460 where D is the diffusion coefficient of slow diffusing Si and Al cations in the melt ($\sim 10^{-14}$ - 10^{-15} $\text{m}^2 \text{s}^{-1}$ at
 461 1,050-1,100 °C; Zhang et al., 2010). λ (2.7 Å) and V (7.59×10^{-5} $\text{m}^3 \text{mol}^{-1}$) are the diameter of the
 462 diffusing building molecules and the molar volume of a pure diopside, respectively (data from
 463 Nascimento et al., 2004). ΔG is the Gibbs free energy of clinopyroxene formation estimated by rhyolite-
 464 MELTS at the experiment conditions (~ 7 -22 kJ mol^{-1} ; Gualda et al., 2012). The parameters f , σ , and α
 465 are the fraction of preferred growth sites at the crystal interface, the crystal-melt surface energy, and the
 466 reduced surface energy, respectively (cf. Nascimento et al., 2004 and references therein). The crystal
 467 growth path modeled through this approach is depicted as green (1,050 °C) and blue (1,100 °C) trends
 468 in Fig. 7. In order to isolate the effect of ΔT , the modeled trends are compared with values of G_{max} (green
 469 and blue diamonds for 1,050 and 1,100 °C, respectively) from decompression and cooling rate

470 experiments conducted over similar relaxation times (i.e., in the order of minutes for ΔPf -1100-2H₂O,
471 ΔPf -1100-5H₂O, ΔPf -1100-H₂O+CO₂, ΔPf -1050-2H₂O, ΔPf -1050-5H₂O, ΔPf -1050-H₂O+CO₂, CR-
472 1050-0.25, CR-1050-0.5). Small values of ΔT from *Experimental Set* ΔPf promote an interface-controlled
473 growth (Fig. 7) and the development of large, euhedral sector-zoned crystals characterized by well-
474 formed prismatic morphologies (Figs. 2 and 4, and Supplementary Material 2). The lack of skeletal
475 shapes and formation of sector-zoned clinopyroxenes indicate sluggish crystallization kinetics typically
476 observed at $\Delta T \leq 30$ °C (Kouchi et al., 1983; Ubide et al., 2019a; Giuliani et al., 2020; Masotta et al.,
477 2020). Sector-zoned crystals have identical three-dimensional atomic configurations, but the surface of
478 each individual growing sector has a specific two-dimensional atomic arrangement (Dowty, 1976 and
479 references therein). Adjacent crystal regions grow simultaneously and form crystallographically
480 nonequivalent faces with distinctively intersectoral chemical variations, with Di-Hd-rich, CaTs-CaTiTs-
481 poor hourglass sectors $\{-1\ 1\ 1\}$ and Di-Hd-poor, CaTs-CaTiTs-rich prism sectors $\{1\ 0\ 0\}$ (Fig. 5). These
482 intersectoral differences emerge only under the effect of small ΔT (Kouchi et al., 1983; Masotta et al.,
483 2020), when slow crystal growth kinetics ensure the attainment of clinopyroxene euhedrality (Fig. 4a).
484 As a consequence, the different types of cation substitutions in the sectors reflect the variable spatial
485 structural distributions of M and T sites as a function of the growth velocity of polyhedral sectors (Dowty,
486 1976 and references therein) rather than the disequilibrium advancement of a skeletal crystal surface via
487 kinetic roughening transition (Sunagawa, 2005).

488 According to the above criteria, Fig. 7 displays thermodynamic modeling paths that confirm
489 transition between interface-controlled and diffusion-controlled growth at ΔT threshold value of ~33 °C.
490 A diffusion-controlled growth regime develops only when large ΔT from *Experimental Set* CR operate
491 in combination with short relaxation times (Fig. 7). The interface kinetics become extremely fast and
492 tiny, anhedral clinopyroxenes crystallize from supersaturated melt regions where nucleation kinetics
493 strongly prevail over the growth (Figs. 2 and 4b, and Supplementary Material 2). Kinetic effects due to
494 different cation diffusivities in the melt overprint the control exercised by the structural sites of the
495 advancing crystal surface (Giuliani et al., 2020). As a result, there is no evident control of crystal
496 structural sites on cation incorporation and precise chemical correlations amongst the zoning patterns of
497 skeletal clinopyroxenes cannot be identified (Kouchi et al., 1983; Masotta et al., 2020).

498

499 4.3 Parameterization of clinopyroxene growth kinetics

500 Growth rates obtained in this study are compared in Fig. 8a with those measured by previous
501 experimental works investigating basaltic and trachybasaltic compositions that ~~virtually~~ reproduce the

502 overall intrinsic variability of rocks from the Monte Maletto Formation (Baker, 2008; Mollo et al., 2013;
503 Pontesilli et al., 2019; Masotta et al., 2020). As pointed out by Bonechi et al. (2020), there is a strong
504 control of melt composition on the crystal growth rate due to polymerization effects caused by an
505 increasing number of tetrahedral sites relative to octahedral sites, thereby enhancing the melt viscosity
506 and lowering the diffusivity of elements in the melt. Accounting also for the major effects of T and H_2O
507 on melt viscosity, all the parameterized experiments were performed at conditions analogous to those
508 estimated for magmas erupted at Mt. Etna volcano (i.e., $P = 0.1\text{-}1,000$ MPa, $T = 1,050\text{-}1,150$ °C, $H_2O =$
509 $0\text{-}4$ wt.%, $fO_2 = NNO+1.5\text{-}NNO+2$, $\Delta T = 75\text{-}233$ °C, and $CR = 0.001\text{-}100$ °C s⁻¹; see the review study of
510 Mollo et al., 2018 and references therein). Fig. 8a shows that G_{max} sensibly decreases of approximately
511 six orders of magnitude, from $\sim 10^{-9}$ to $\sim 10^{-15}$ mm s⁻¹, as the relaxation time increases from 0.08 to 72 h
512 (Fig. 8a). Statistical calculations were carried out on the experimental data set with the Statgraphics
513 Centurion 18[®] algorithm (Statpoint Technologies, Inc., Warrenton, VA, USA) by running a weighted
514 least square (WLS) regression analysis. While in ordinary least square (OLS) regressions the standard
515 deviation (σ) of error is assumed constant over all values of the explanatory variable, in WLS regressions
516 the efficiency of estimation is maximized by giving to each data its proper amount of influence (i.e.,
517 weight w) over the estimate. This is especially important in modeling of logarithmic data sets that are
518 susceptible to uncertainties associated with the linearization of the model (i.e., heteroskedasticity; Hair
519 et al., 1995). On this basis, error minimization is attained by 1) incorporating weights into the fitting
520 criterion and 2) performing Monte Carlo propagation of errors (Ratkowsky, 1990). The general form of
521 WLS model is written in matrix notation as:

522

$$523 \mathbf{Y} = \mathbf{X}\boldsymbol{\beta} + \boldsymbol{\varepsilon} \quad (10)$$

524

525 where $\mathbf{Y} = (n \times 1)$ vector of y observations, $\mathbf{X} = (n \times k)$ matrix of x variables, and $\boldsymbol{\beta} = (k \times 1)$ vector of β
526 regression coefficients. The $\boldsymbol{\varepsilon} = (n \times 1)$ vector of random errors ε is expressed as $(\mathbf{0}, \boldsymbol{\sigma}^2\mathbf{W})$. In OLS, ε has
527 mean equals to zero and variance close to the square of the standard deviation [$var(\varepsilon) = \sigma^2$]. Conversely,
528 in WLS, ε does not have constant variance [$var(\varepsilon) = \sigma^2/w$] and the weight given to each observation is
529 inversely proportional to the variance of the explanatory variable. \mathbf{W} represents an $(n \times n)$ diagonal matrix
530 with diagonal entries corresponding to weights and $\mathbf{Var}(\boldsymbol{\varepsilon}) = \mathbf{W}^{-1}\boldsymbol{\sigma}^2$. The solution of Eqn. (10) is:

531

$$532 \boldsymbol{\beta}^* = \frac{\mathbf{X}^T \mathbf{W} \mathbf{Y}^*}{\mathbf{X}^T \mathbf{W} \mathbf{X}} \quad (11)$$

533

534 where β^* and Y^* are estimates of β and Y , respectively, and X^T is the transpose of matrix X . WLS
535 regression of experimental data displayed in Fig. 8a have the following form:

536

$$537 \ln G_{max} = \beta_0 + \beta_1 \ln t_{max} \quad (12)$$

538

539 The best predicting model for G_{max} has been calculated by optimizing the weighted fitting criterion and
540 estimating the variance of the data set for each fixed covariate vector in Eqn. (11). This statistical
541 approach allows to downweight outliers and reduce their impact on the overall model. The least square
542 minimization of Eqn. (12) yields $\beta_0 = -5.512 (\pm 0.041 \sigma_{\beta_0})$ and $\beta_1 = -0.778 (\pm 0.012 \sigma_{\beta_1})$. The coefficient
543 of determination (R^2), standard error of estimate ($SEE_{G_{max}}$), and mean absolute error (ε) are 0.977, 0.242,
544 and 0.181, respectively. As a further error test, the regression constants β_0 and β_1 have been also
545 recalculated by perturbing Eqn. (12) via Monte Carlo simulations over a normal distribution with the
546 mean centered on the original value of G_{max} and with deviation close to $SEE_{G_{max}}$ (Hair et al., 1995). After
547 generating 1,000 sets of hypothetical regression coefficients, results from probability density functions
548 confirm data from least square minimization. Therefore, it is calculated that ~68% of β_0 (Fig. 8b) and β_1
549 (Fig. 8c) have uncertainties of $\pm 0.039 \sigma_{\beta_0}$ and $\pm 0.011 \sigma_{\beta_1}$, respectively. Since most of the calibration data
550 were obtained at 0 and 2 wt.% H₂O contents in both the present study and previous works, WLS
551 regressions have been replicated on two distinct data sets for anhydrous (0 wt.% H₂O) and hydrous (2
552 wt.% H₂O) experiments. These calculations yield very similar regression coefficients ($^{anhydrous} \beta_0 = -5.589$
553 vs. $^{hydrous} \beta_0 = -5.521$, as well as $^{anhydrous} \beta_1 = -0.771$ vs. $^{hydrous} \beta_1 = -0.778$) and errors of estimate
554 ($^{anhydrous} SEE_{G_{max}} = 0.251$ vs. $^{hydrous} SEE_{G_{max}} = 0.244$). Attainment of comparable regression coefficients
555 points out that the kinetic control of H₂O on G_{max} (Fig. 6a) and crystal content (Fig. 3a) is almost
556 equivalent to that imposed by temperature. For example, at constant T , G_{max} increases by 20% as the
557 melt-H₂O content increases from 0 to 5 wt.%. Analogously, at constant H₂O concentration, G_{max}
558 increases by 18% as T increases from 1,050 to 1,100 °C. As previously observed by Pontesilli et al.
559 (2019), the magnitude of G_{max} is mostly dictated by the time of crystal growth (Fig. 6b) that becomes
560 increasingly more effective with increasing crystal size (L_{max}) and textural maturation (S_v^P).

561 Recalling the crystal size distribution (CSD) theory, the crystal nucleation rate is related to the
562 growth rate as $J = N_0 \times G$. By assuming $G = G_{max}$ and $\tau = t_{max}$, we can substitute Eqn. (12) into $m = 1 /$
563 $(G \times \tau)$ and then rearrange this algebraic expression to isolate the crystallization time of clinopyroxene:

564

$$565 \quad G_{\max} = t_{\max}^{\beta_1} \exp \beta_0, \quad (13)$$

566

$$567 \quad m = -\frac{1}{\left[t_{\max}^{(\beta_1+1)} \exp \beta_0 \right]}, \text{ and} \quad (14)$$

568

$$569 \quad t_{\max} = \left[-\frac{1}{m \exp \beta_0} \right]^{\frac{1}{\beta_1+1}} \quad (15)$$

570

571 The overall uncertainty associated with the estimate of t_{\max} has been determined by propagating into Eqn.
572 (15) the values of $SEE_{G_{\max}}$, σ_{β_0} , and σ_{β_1} via Monte Carlo simulations. Density estimations indicate that
573 the uncertainty of t varies from 22% to 28%, with an average close to 26% (Fig. 8d).

574

575 4.4. Application to magma dynamics at Mt. Etna volcano

576 Mt. Etna is one of the most studied and monitored volcanoes in the world. The persistent eruptive
577 activity of Mt. Etna ~~threats~~ the populations living in its shadow, also causing regional climate changes in
578 Sicily and the temporary closure of the Fontanarossa International airport of Catania. The plumbing
579 system is governed by frequent input and mixing of primitive, volatile-rich magmas rising from a deeper
580 (~10 km) storage region into shallower reservoirs (3-5 km) and, occasionally, ponding within the
581 volcanic edifice (0.5-2.5 km; Patanè et al., 2003; Corsaro et al., 2009; Ubide and Kamber, 2018; Mollo
582 et al., 2018). Abundant volatile exsolution and degassing are the key mechanisms controlling mineral
583 and melt compositions, degree of crystallization, magma ascent velocity, and eruptive style (Armienti et
584 al., 2007; Lanzafame et al., 2013). Magma can be erupted either quickly through deep dykes feeding
585 eccentric eruptions (i.e., bypassing the central conduits) or gradually through the central conduits feeding
586 shallow reservoirs (Ubide and Kamber, 2018).

587 A cyclic fountaining activity **interested** the New Southeast Crater (NSEC) in 2011–2012 and
588 2013, including normal paroxysmal sequences and energetic episodes with high eruption columns (7–8
589 km above the vent). A detailed multi-disciplinary data set referring to these eruptions can be found in
590 literature, including ~~also~~ mineral and melt compositions, volcanological constraints, thermal mapping,
591 and structural surveys (Andronico et al., 2005; Ferlito et al., 2009, 2012; Mollo et al., 2015b, 2018;
592 Perinelli et al., 2016; Giuffrida and Viccaro, 2017; Giuffrida et al., 2018; Giacomoni et al., 2018). In this
593 study, we focus on clinopyroxene microphenocrysts and microlites from fourteen 2011-2012 scoria clasts

594 that are representative of 12/01/2011, 18/02/2011, 10/04/2011, 12/05/2011, 30/07/2011, 20/08/2011,
595 29/08/2011, 08/09/2011, 15/11/2011, 05/01/2012, 04/03/2012, 18/03/2012, 01/04/2012, and 24/04/2012
596 lava fountains (Supplementary Material 3). These samples have variable vesicularity (15-30%) and
597 porphyritic index (30-60%), but a uniform phase assemblage of olivine + clinopyroxene + plagioclase +
598 titanomagnetite + glass (see Supplementary Material 3 and Giacomoni et al., 2018 for a detailed
599 petrographic description). By analyzing cation redistributions in 2011-2012 clinopyroxenes and
600 titanomagnetites, Mollo et al. (2015b) documented the ability of microphenocrysts and microlites to
601 record variable undercooling histories comprised between the sub-liquidus temperature of the magmatic
602 reservoir and the closure temperature of crystal growth, when the kinetics and energetics of solidification
603 were rapidly frozen-in at the time of eruption.

604 The saturation conditions of clinopyroxenes from 2011-2012 lava fountains, prior to dynamic
605 ascent of magma towards the surface, have been estimated in this study through the integrated P - T - H_2O
606 model of Mollo et al. (2018) specifically designed to Etnean minerals and their host magmas
607 (Supplementary Material 4). The model uncertainty is minimized by adjusting the P - T - H_2O estimates
608 within the calibration errors of the barometer (± 150 MPa), thermometer (± 20 °C), and hygrometer (± 0.45
609 wt.% H_2O), in order to reduce the difference (Δ) between measured and predicted equilibrium values of
610 Kd_{Fe-Mg} (Fe-Mg exchange partition coefficient; Putirka, 2008), K_{Na} (Na partition coefficient; Blundy et
611 al., 1995), and $DiHd$ (diopside + hedenbergite; Mollo et al., 2013). These correction criteria and
612 probability density functions are applied to microphenocryst and bulk rock compositions (Supplementary
613 Material 4), providing the most reliable near-equilibrium conditions for clinopyroxene saturation at
614 ~ 210 - 260 MPa (i.e., ~ 8 - 10 km, presuming a continental crust density of 2.6 g cm^{-3} ; Armienti et al., 2013),
615 $\sim 1,070$ - $1,080$ °C, and ~ 2.2 - 2.4 wt.% H_2O (Fig. 9). Notably, the estimated pressure range matches with
616 magma storage at an intermediate depth of 7 - 13 km (Murru et al., 1999) and within a major aseismic
617 high P-wave velocity body extending down to 18 km (Aloisi et al., 2002).

618 Fig. 10 shows CSD curves of 2011-2012 clinopyroxenes, with kinked concave-up shapes and
619 marked changes in slope, from a shallower gradient in the larger crystals to a steeper gradient in the
620 smaller ones (Burney et al., 2020). Regression coefficients determined for microphenocrysts (m from -
621 13.589 to -16.914 mm^{-1} and N_0 from 8.177 to 10.358 mm^{-4}) and microphenocrysts (m from -45.981 to -
622 93.140 mm^{-1} and N_0 from 13.796 to 16.764 mm^{-4}) are characteristically different (Table 2). Coherently,
623 the systematic kink of CSD curves attests the occurrence of distinct crystal size distributions for
624 microphenocrysts ($L \geq 0.1$ mm) and microlites ($L < 0.1$ mm). In a few samples the kink shifts at 0.14 mm
625 because of the higher crystallinity of the erupted products (Cashman and Marsh 1988; Higgins 1996).

626 These kinked shape trends are generally attributed to variable crystal growth rates and undercooling
627 histories of magmas during ascent along different portions of the plumbing system and volcanic conduit,
628 without any gain or loss from/to external magma batches (Kirkpatrick, 1981, 1983; Maaloe et al., 1989;
629 Armienti et al., 1994; Armienti, 2008). In this context, $N(L)$ vs. L trajectories displayed in Fig. 10 and
630 their regression coefficients (Table 2) are principally the result of different crystallization regime upon
631 the P - T - H_2O array experienced by dynamically erupted magmas (Armienti et al., 2013).

632 By applying Eqn. (15) to the slope of each CSD curve, we have quantified the crystallization time
633 recorded by the textural evolution of 2011-2012 clinopyroxenes. Results from calculations are listed in
634 Table 2 and return values of t_{max} ranging from $\sim 1.4 \pm 0.3$ to $\sim 33.4 \pm 8$ min and from $\sim 50.7 \pm 13$ to $\sim 136.2 \pm 35$
635 h for microlite and microphenocryst populations, respectively. The low magnitude of t_{max} measured for
636 microlites testifies to fast kinetic effects and rapid crystal growth regimes, when magma acceleration
637 within the uppermost part of the conduit and large ΔT lead to strong melt supersaturation (Armienti,
638 2008). According to this proposition, fluid mechanic mechanisms governing magma ascent indicate that,
639 upon abundant volatile exsolution within a narrow degassing path, the volume expansion of magma by
640 the growth of gas bubbles is balanced by an increasing acceleration towards the surface (Gonnermann
641 and Manga, 2013). Conversely, the high magnitude of t_{max} derived for microphenocrysts indicates
642 sluggish kinetic effects associated with small ΔT and slow crystal growth regimes from more relaxed
643 melts. Evidently, at greater depths and within the plumbing system of Mt. Etna volcano, clinopyroxene
644 microphenocrysts have more time to grow and equilibrate with the feeding melt under steady-state
645 conditions (Armienti et al., 2013).

646 We emphasize that values of t_{max} are intrinsically related to the kinetic aspects and
647 thermodynamics of clinopyroxene growth. Therefore, caution should be exercised in comparing the
648 magnitude of t_{max} with the time scale of magma dynamics derived by numerical modeling of volcanic
649 conduit processes (e.g., La Spina et al., 2016, 2021; Polacci et al., 2019) and/or time scales from
650 elemental diffusion (e.g., Giuffrida et al., 2018; Ubide and Kamber, 2018). The corollary is that the
651 crystal growth will never occur when a full thermodynamic equilibrium (i.e., a minimum energy state)
652 is achieved throughout the crystal-melt interface. There is an energy barrier to overcome in order to
653 promote imbalance between the attachment and detachment energies of cations at the crystal-melt
654 interface. This excess energy is attained by melt supersaturation, when the thermodynamic driving force
655 is higher than a critical threshold above which crystal growth takes place (Sunagawa, 2005). At large ΔT ,
656 such as those typically occurring during rapid ascent of magma within a volcanic conduit, the effective
657 mechanism controlling clinopyroxene kinetic growth depends on the slow diffusivity of Si and Al in the

658 melt with respect to Ca and Mg. The addition of network-former species to the growing surface of crystals
659 is the rate-controlling step for the textural maturation of clinopyroxene (Mollo and Hammer, 2017).
660 Moreover, since the strength of the ^TSi–O bonds in the melt is greater than that of ^TAl–O bonds
661 (Kirkpatrick, 1983), the transfer rate of incompatible cations (i.e., Al + Ti) from the melt to the crystal
662 surface is much more facilitated than that of compatible elements (i.e., Ca + Mg; Mollo et al., 2010,
663 2012(a o b); Pontesilli et al., 2019; Masotta et al., 2020). According to these kinetic principles, G_{max} and
664 t_{max} are inextricably interrelated to the morphological stability of the crystal-melt interface throughout
665 the growth process (Sunagawa, 2005). The crystal-melt interface is the locus where growth or dissolution
666 take place upon dynamic changes of P - T - H_2O during magma ascent towards the surface and upon
667 decompression-cooling paths. Melt supersaturation causes morphological instability of the crystal and
668 shifts from polyhedral to hopper to dendritic forms, by imposing temperature and concentration gradients
669 at the interface (Sunagawa, 2005).

670 According to the above considerations, the magnitude of G_{max} and t_{max} mostly depends on 1)
671 morphological instability as a function of attachment/detachment energies of cations with increasing ΔT
672 and 2) concentration gradients in the melt next to the advancing crystal surface and disequilibrium uptake
673 of incompatible cations within the lattice site (Pontesilli et al., 2019; Masotta et al., 2020). However, it
674 is interesting to note that values of t_{max} (~1-41 min; Table 2) measured for 2011-2012 clinopyroxene
675 microlites are consistent with the numerical analysis of magma ascent times within volcanic conduits
676 with either cylindrical or dyke geometries, and based on the entire 1995–2019 explosive activity of Mt.
677 Etna that produced, among other products, significant ash emissions (Polacci et al., 2019). This analysis
678 yields ascent time minimum (~2.5 min) at the center of the conduit and maximum (~25 min) the conduit
679 walls, corresponding to ~1% of the total magma rising within the conduit. Similarly, the ascent time of
680 magma within a dyke ranges from ~3.3 min to ~33 min, with this latter quantity representative of less
681 than 0.4% of the total magma (Polacci et al., 2019). According to La Spina et al. (2021), lava fountaining
682 at Mt. Etna consists of an eruptive style distinct from effusive and explosive eruptions, as the result of
683 rapid magma ascent with most of fragmentation above the vent rather than within the conduit. Magma
684 ascent times of ~40 min determined by La Spina et al. (2021) are in the same order of magnitude of t_{max}
685 calculated for some 2011-2012 microlites and microphenocrysts from this study.

686 A conceptual model of open conduit dynamics at Mt. Etna is schematized in Fig. 11. Most of the
687 clinopyroxene microlite crystallization occurs within the uppermost segment of the volcanic conduit
688 under the effect of large ΔT and short t_{max} (Fig. 11). This fast disequilibrium time is also comparable with
689 that (< 60 min) estimated for plagioclase during dynamic ascent of magma and under strong

690 disequilibrium conditions driven by abundant volatile exsolution (La Spina et al., 2016). *In-situ*
691 experiments carried out on a typical Etnean trachybasalt reveal that $\Delta T = 60\text{-}140$ °C drive exceptionally
692 rapid crystallization of plagioclase and clinopyroxene microlites in several minutes, also inducing a step
693 change in viscosity that may trigger magma fragmentation (Arzilli et al., 2019). Moreover, because of
694 rapid fractionation of lithium between melt and fluid during magma degassing, the decrease in Li
695 concentration in plagioclase by diffusion corresponds to magma ascent time scales variable from 0.2 to
696 3 min for paroxysmal sequences (Giuffrida et al., 2018). This syn-eruptive stage of magma is outlined
697 by t_{max} of $\sim 1\text{-}3$ min calculated for 2011-2012 clinopyroxene microlites (Fig. 11), as well as by rapid
698 decompression (12 MPa min^{-1}) and cooling experiments (12 °C min^{-1}) of Arzilli et al. (2019) showing
699 that abundant clinopyroxene microlite crystallization occurs in only 5 min at $\Delta T > 100$ °C. Considering
700 that most of disequilibrium crystallization takes place at ~ 1.5 km below the vent (cf. La Spina et al.,
701 2016, 2021), we derive maximum magma ascent rates of $1\text{-}23 \text{ m s}^{-1}$ (Table 2 and Fig. 11). These estimates
702 are statistically comparable with syn-eruptive ascent rates of $\sim 3 \text{ m s}^{-1}$ determined for mild lava
703 fountaining activity at Mt. Etna, Stromboli, and Kilauea (Arzilli et al., 2019 and references therein), as
704 well as for syn-eruptive ascent rates measured for shallow subvolcanic magma storage zones (depth ≤ 10
705 km) feeding more silicic explosive eruptions worldwide ($\sim 0.5\text{-}50 \text{ m s}^{-1}$; Cassidy et al., 2018).

706 Notably, the compositional difference between the initial melt and the final three-dimensional
707 structural arrangement of the crystal requires that stable nuclei can form only when the local
708 configuration of molecular units attains a critical dimension (Vetere et al., 2015). As the microlite
709 crystallization increases during ascent of magma within the conduit, the residual melt composition
710 becomes progressively more differentiated (i.e., $\text{SiO}_2\text{-Na}_2\text{O}$ -rich and CaO-MgO -poor) favoring the
711 enlargement of plagioclase stability field (i.e., albite end-member) at the expense of clinopyroxene (i.e.,
712 diopside end-member). For this reason, at very large ΔT , the kinetic growth of 2011-2012 clinopyroxene
713 microlites does not return magma ascent rates $> 23 \text{ m s}^{-1}$ (Fig. 11), such as those related to strong degassing
714 processes governing Li diffusion in plagioclase ($\sim 43 \text{ m s}^{-1}$; Giuffrida et al., 2018) and further magma
715 acceleration at the vent ($\sim 75 \text{ m s}^{-1}$; La Spina et al., 2021).

716 Differently from shallow conduit and vent dynamics, values of t_{max} ($\sim 38\text{-}171$ h; Table 2)
717 calculated for 2011-2012 clinopyroxene microphenocrysts are orders of magnitude greater than the very
718 fast crystallization history recorded by microlites. Evidently, the growth of microphenocrysts does not
719 represent the timing of eruption within the upper conduit or immediately before ejection from the vent,
720 where strong supersaturation phenomena are driven by fast cooling, decompression, and degassing of
721 magma (Fig. 11). Rather, most of microphenocryst growth is governed by a small ΔT and long t_{max} at

722 depth (Fig. 11), where crystallization kinetics are slow and the crystal surface has enough time to develop
723 polyhedral morphology (Armienti et al., 2013). Moreover, there is no systematic change of t_{max} with the
724 1) 2011-2012 paroxysmal phase duration, 2) Strombolian activity preceding lava fountaining, and 3)
725 associated seismic signals or volcanic tremors (data from the multidisciplinary reports of the INGV
726 Osservatorio Etneo available at www.ct.ingv.it). This suggests that the onset of microphenocryst growth
727 takes place at the early saturation condition of clinopyroxene and under a near-equilibrium crystallization
728 state corresponding to the main storage region of magma at ~8-10 km of depth. It is also not excluded
729 that microphenocryst crystallization continues via open system processes governed by the invasion of
730 the plumbing system with fresh magma (Fig. 11). Time scales from this study closely match with those
731 (~17-168 h) derived by Ubide and Kamber (2018) for the development of Cr zoning in clinopyroxene
732 caused by continuous magma recharge and mixing events at depth of ~10 km (Fig. 11). Under such
733 conditions, both volatile exsolution and crystallization are low, bubble expansion and magma buoyancy
734 are limited, and the slow upward migration of magma provides more time for mineral-melt-fluid
735 equilibration (e.g., Cassidy et al., 2018). Ubide and Kamber (2018) estimated magma ascent rates of
736 0.02-0.17 m s⁻¹ that are analogous to those (0.02-0.07 m s⁻¹; Table 2) determined for the growth of 2011-
737 2012 clinopyroxene microphenocrysts. Therefore, differently from the fast acceleration of magma within
738 the conduit, open system dynamics at depth require longer time periods for the migration of magma
739 through interconnected storage regions (Fig. 11). This conclusion is supported by similar estimates
740 obtained through different methodologies based on cation redistributions in minerals (0.01-0.31 m s⁻¹;
741 Mollo et al., 2015b) and geophysical signals (0.04-0.4 m s⁻¹; Aloisi et al., 2006) at Mt. Etna volcano, as
742 well as by authors investigating other volcanic settings worldwide, such as Hawaii (0.01–0.04 m s⁻¹;
743 Rutherford, 2008; Gonnermann and Manga, 2013), Unzen (0.01–0.07 m s⁻¹; Toramaru et al., 2008) and
744 Mount St. Helens (0.01–0.15 m s⁻¹; Rutherford and Hill, 1993).

745

746 5. Conclusions

747 Clinopyroxene growth kinetics have been experimentally investigated and parameterized under a
748 broad range of isothermal-isobaric, decompression, and cooling rate conditions, representative of
749 variable magma crystallization paths at Mt. Etna volcano. Through this approach, the following main
750 conclusions can be drawn:

- 751 1) the texture of clinopyroxene is greatly controlled by supersaturation and relaxation phenomena
752 resulting from P - T - H_2O changes;

- 753 2) crystal euhedrality is maintained either under isothermal-isobaric or slow-to-fast decompression
754 conditions, with the main difference represented by the development of sector-zoned
755 clinopyroxenes during melt decompression;
- 756 3) as the relaxation time increases, the crystal growth rate radically decreases, whereas the crystal
757 euhedrality increases;
- 758 4) thermodynamic modeling suggests that the transition between interface-controlled and diffusion-
759 controlled growth arises at undercooling higher than ~ 33 °C;
- 760 5) below this threshold value, sluggish crystallization kinetics lead to the formation of sector-zoned
761 clinopyroxenes, with Di-Hd-rich, CaTs-CaTiTs-poor hourglass sectors $\{-1\ 1\ 1\}$ and Di-Hd-poor,
762 CaTs-CaTiTs-rich prism sectors $\{1\ 0\ 0\}$ typically observed at Mt. Etna volcano;
- 763 6) by integrating experimental textural data and the algebraic expression of crystal size distribution
764 (CSD), the crystallization time of clinopyroxene can be parameterized as a function of growth
765 rate;
- 766 7) for the case of 2011-2012 lava fountains, results from calculations return time scales variable
767 from $\sim 10^0$ - 10^1 min and $\sim 10^1$ - 10^2 h for microlite and microphenocryst populations, respectively;
- 768 8) while shorter time scales of microlites testify to fast kinetic effects due to large undercoolings
769 during magma acceleration in the uppermost part of the volcanic conduit, longer time scales of
770 microphenocrysts are associated with near-equilibrium crystallization due to small undercoolings
771 at depth;
- 772 9) we conclude that fast ascent rates of magmas ($\sim 10^0$ - 10^1 m s⁻¹) lead to disequilibrium growth of
773 microlites and supersaturation effects due to strong degassing and cooling before eruption from
774 the vent. In contrast, slow ascent rates of magmas ($\sim 10^{-2}$ m s⁻¹) favor near-equilibrium
775 crystallization of microphenocrysts over longer time periods and within the interconnected
776 storage regions that characterize the plumbing system architecture of Mt. Etna volcano.

777

778 **Acknowledgements**

779 Authors thanks A. Vona for his kind help with crystal size distribution (CSD) analysis.

780

781 **References**

782 Aloisi, M., Cocina, O., Neri, G., Orecchio, B., Privitera, E., 2002. Seismic tomography of the crust
783 underneath the Etna volcano, Sicily. *Phys. Earth Planet. Inter.* 134, 139–155.

784 Aloisi, M., Bonaccorso, A., Gambino, S., 2006. Imaging composite dike propagation (Etna, 2002
785 case). *J. Geophys. Res.* 111.

786 Andronico, D., Branca, S., Calvari, S., Burton, M., Caltabiano, T., Corsaro, R.A., Del Carlo, P.,
787 Garfi, G., Lodato, L., Miraglia, L., Murè, F., Neri, M., Pecora, E., Pompilio, M., Salerno, G., Spampinato,
788 L., 2005. A multi-disciplinary study of the 2002-03 Etna eruption: insights into a complex plumbing
789 system. *Bull Volcanol* 67, 314–330.

790 Armienti, P., Pareschi, M.T., Innocenti, F., Pompilio, M., 1994. Effects of magma storage and ascent
791 on the kinetics of crystal growth. *Contr. Mineral. and Petrol.* 115, 402–414.

792 Armienti, P., Francalanci, L., Landi, P., 2007. Textural effects of steady state behaviour of the
793 Stromboli feeding system. *J. Volcanol. Geotherm. Res.* 160, 86–98.

794 Armienti, P., 2008. Decryption of Igneous Rock Textures: Crystal Size Distribution Tools. *Rev*
795 *Mineral Geochem* 69, 623–649.

796 Armienti, P., Perinelli, C., Putirka, K.D., 2013. A New Model to Estimate Deep-level Magma Ascent
797 Rates, with Applications to Mt. Etna (Sicily, Italy). *J. Petrol.* 54, 795–813.

798 Arzilli, F., Fabbrizio, A., Schmidt, M.W., Petrelli, M., Maimaiti, M., Dingwell, D.B., Paris, E.,
799 Burton, M., Carroll, M.R., 2018. The effect of diffusive re-equilibration time on trace element
800 partitioning between alkali feldspar and trachytic melts. *Chem. Geol.* 495, 50–66.

801 Arzilli, F., La Spina, G., Burton, M.R., Polacci, M., Le Gall, N., Hartley, M.E., Di Genova, D., Cai,
802 B., Vo, N.T., Bamber, E.C., Nonni, S., Atwood, R., Llewellyn, E.W., Brooker, R.A., Mader, H.M., Lee,
803 P.D., 2019. Magma fragmentation in highly explosive basaltic eruptions induced by rapid crystallization.
804 *Nat. Geosci.* 12, 1023–1028.

805 Baker, D.R., 2008. The fidelity of melt inclusions as records of melt composition. *Contrib Mineral*
806 *Petrol* 156, 377–395.

807 Blundy, J.D., Falloon, T.J., Wood, B.J., Dalton, J.A., 1995. Sodium partitioning between
808 clinopyroxene and silicate melts. *J. Geophys. Res. Solid Earth* 100, 15501–15515.

809 Bonechi, B., Perinelli, C., Gaeta, M. Clinopyroxene growth rates at high pressure: constraints on
810 magma recharge of the deep reservoir of the Campi Flegrei Volcanic District (south Italy). *Bull Volcanol*
811 82, 5.

812 Botcharnikov, R.E., Almeev, R.R., Koepke, J., Holtz, F., 2008. Phase Relations and Liquid Lines of
813 Descent in Hydrous Ferrobasalt--Implications for the Skaergaard Intrusion and Columbia River Flood
814 Basalts. *J. Petrol.* 49, 1687–1727.

815 Burkhard, D.J.M., 2005. Nucleation and growth rates of pyroxene, plagioclase, and Fe-Ti oxides in
816 basalt under atmospheric conditions. *European Journal of Mineralogy* 17, 675–686.

817 Burney, D., Peate, D.W., Riishuus, M.S., Ukstins, I.A., 2020. Reconstructing the plumbing system
818 of an off-rift primitive alkaline tuya (Vatnafell, Iceland) using geothermobarometry and CSDs. *J.*
819 *Volcanol. Geotherm. Res.* 399, 106914.

820 Cashman, K.V., Marsh, B.D., 1988. Crystal size distribution (CSD) in rocks and the kinetics and
821 dynamics of crystallization II: Makaopuhi lava lake. *Contr. Mineral. and Petrol.* 99, 292–305.

822 Cashman, K.V., 1990. Textural constraints on the kinetics of crystallization of igneous
823 rocks. *Rev. Mineral.* 24, 259–314.

824 Cassidy, M., Manga, M., Cashman, K., Bachmann, O., 2018. Controls on explosive-effusive
825 volcanic eruption styles. *Nat Commun* 9.

826 Corsaro, R.A., Civetta, L., Di Renzo, V., Miraglia, L., 2009. Petrology of lavas from the 2004–2005
827 flank eruption of Mt. Etna, Italy: inferences on the dynamics of magma in the shallow plumbing system.
828 *Bull. Volcanol.* 71, 781–793.

829 Di Stefano, F., Mollo, S., Ubide, T., Petrone, C.M., Caulfield, J., Scarlato, P., Nazzari, M.,
830 Andronico, D., Del Bello, E., 2020. Mush cannibalism and disruption recorded by clinopyroxene
831 phenocrysts at Stromboli volcano: New insights from recent 2003–2017 activity. *Lithos* 360–361,
832 105440.

833 Dowty, E., 1976. Crystal structure and crystal growth: II. Sector zoning in minerals. *Am. Mineral.*
834 61, 460–469.

835 Duan, X., 2014. A general model for predicting the solubility behavior of H₂O-CO₂ fluids in silicate
836 melts over a wide range of pressure, temperature and compositions. *Geochim. Cosmochim. Acta* 125,
837 582–609. <http://dx.doi.org/10.1016/j.gca.2013.10.018>.

838 Ferlito, C., Coltorti, M., Cristofolini, R., Giacomoni, P.P., 2009. The contemporaneous emission of
839 low-K and high-K trachybasalts and the role of the NE Rift during the 2002 eruptive event, Mt. Etna,
840 Italy. *Bull Volcanol* 71, 575–587.

841 Ferlito, C., Viccaro, M., Nicotra, E., Cristofolini, R., 2012. Regimes of magma recharge and their
842 control on the eruptive behaviour during the period 2001–2005 at Mt. Etna volcano. *Bull Volcanol* 74,
843 533–543.

844 Giacomoni, P.P., Coltorti, M., Mollo, S., Ferlito, C., Braiato, M., Scarlato, P., 2018. The 2011–2012
845 paroxysmal eruptions at Mt. Etna volcano: Insights on the vertically zoned plumbing system. *J. Volcanol.*
846 *Geotherm. Res.* 349, 370–391.

847 Giordano, D., Nichols, A.R.L., Dingwell, D.B., 2005. Glass transition temperatures of natural
848 hydrous melts: a relationship with shear viscosity and implications for the welding process. *J. Volcanol.*
849 *Geotherm. Res.* 142, 105–118.

850 Giuffrida, M., Viccaro, M., 2017. Three years (2011–2013) of eruptive activity at Mt. Etna: Working
851 modes and timescales of the modern volcano plumbing system from micro-analytical studies of crystals.
852 *Earth Sci Rev* 171, 289–322.

853 Giuffrida, M., Viccaro, M., Ottolini, L., 2018. Ultrafast syn-eruptive degassing and ascent trigger
854 high-energy basic eruptions. *Sci Rep* 8.

855 Giuliani, L., Iezzi, G., Vetere, F., Behrens, H., Mollo, S., Cauti, F., Ventura, G., Scarlato, P., 2020.
856 Evolution of textures, crystal size distributions and growth rates of plagioclase, clinopyroxene and spinel
857 crystallized at variable cooling rates from a mid-ocean ridge basaltic melt. *Earth Sci Rev* 204, 103165.

858 Gonnermann, H.M., Manga, M., 2013. Dynamics of magma ascent in the volcanic conduit. In:
859 Fagents, S.A., Gregg, T.K.P., Lopes, R.M.C. (Eds.), *Modeling Volcanic Processes*. Cambridge Univ
860 Press, pp.55–84.

861 Gualda, G.A., Ghiorso, M.S., Lemons, R.V., Carley, T. L., 2012. Rhyolite-MELTS: a modified
862 calibration of MELTS optimized for silica-rich, fluid-bearing magmatic systems. *J. Petrol.* 53, 875–890.

863 Hammer, J.E., 2008. Experimental Studies of the Kinetics and Energetics of Magma Crystallization.
864 *Rev Mineral Geochem* 69, 9–59.

865 Hammer, J.E., 2006. Influence of fO₂ and cooling rate on the kinetics and energetics of Fe-rich
866 basalt crystallization. *Earth Planet. Sci. Lett.* 248, 618–637.

867 Hammer, J., Jacob, S., Welsch, B., Hellebrand, E., Sinton, J., 2016. Clinopyroxene in postshield
868 Haleakala ankaramite: 1. Efficacy of thermobarometry. *Contrib Mineral Petrol* 171.

869 Hair Jr., J.F., Anderson, R.E., Tatham, R.L., Black, W.C., 1995. *Multivariate Data Analysis*. 3rd ed.
870 Macmillan, New York (742 pp.).

871 Higgins, M.D., 1996. Magma dynamics beneath Kameni volcano, Thera, Greece, as revealed by
872 crystal size and shape measurements. *J. Volcanol. Geotherm. Res.* 70, 37–48.

873 Higgins, M.D., 2000. Measurement of crystal size distributions. *Am. Mineral.* 85, 1105–1116.

874 Ishibashi, H., 2013. Spinel–melt oxygen barometry: a method and application to Cenozoic alkali
875 basaltic magmas from the Higashi–Matsuura district, NW Kyushu, Japan. *Geosci. Repts.* 40, 21–32.

876 Karamanov, A., Pisciella, P., Pelino, M., 2000a. The crystallisation kinetics of iron rich glass in
877 different atmospheres. *J. Eur. Ceram. Soc.* 20, 2233–2237.

878 Kirkpatrick, R.J., 1981. Kinetics of crystallization of igneous rocks. In: Lasaga, A.C., Kirkpatrick,
879 R.J. (Eds.), *Reviews in Mineralogy* 8. pp. 321–395.

880 Kirkpatrick, R.J., 1983. Theory of nucleation in silicate melts. *Am. Mineral.* 68, 66–77.

881 Kostov, I., Kostov, R.I., 1999. *Crystal Habits of Minerals*. Bulgarian Academic Monographs,
882 Sophia.

883 Kouchi, A., Sugawara, Y., Kashima, K., Sunagawa, I., 1983. Laboratory growth of sector zoned
884 clinopyroxenes in the system $\text{CaMgSi}_2\text{O}_6\text{-CaTiAl}_2\text{O}_6$. *Contrib. Mineral. Petrol.* 83, 177–184.

885 Lanzafame, G., Mollo, S., Iezzi, G., Ferlito, C., Ventura, G., 2013. Unraveling the solidification path
886 of a pahoehoe “cicirara” lava from Mount Etna volcano. *Bull Volcanol* 75.

887 La Spina, G., Burton, M., de’ Michieli Vitturi, M., Arzilli, F., 2016. Role of syn-eruptive plagioclase
888 disequilibrium crystallization in basaltic magma ascent dynamics. *Nat Commun* 7.

889 La Spina, G., Arzilli, F., Llewellyn, E.W., Burton, M.R., Clarke, A.B., de’ Michieli Vitturi, M.,
890 Polacci, M., Hartley, M.E., Di Genova, D., Mader, H.M., 2021. Explosivity of basaltic lava fountains is
891 controlled by magma rheology, ascent rate and outgassing. *Earth Planet. Sci. Lett.* 553, 116658.

892 Lasaga, A.C., 1998. *Kinetic Theory in the Earth Sciences*. Princeton University Press, Princeton,
893 New York.

894 Lofgren, G.E., 1974. An experimental study of plagioclase morphology: isothermal crystallization.
895 *Am. J. Sci.* 264, 243–273.

896 Maaløe, S., Tumyr, O., James, D., 1989. Population density and zoning of olivine phenocrysts in
897 tholeiites from Kauai, Hawaii. *Contr. Mineral. and Petrol.* 101, 176–186.

898 Marsh, B.D., 1988. Crystal size distribution (CSD) in rocks and the kinetics and dynamics of
899 crystallization. *Contr. Mineral. and Petrol.* 99, 277–291.

900 Masotta, M., Pontesilli, A., Mollo, S., Armienti, P., Ubide, T., Nazzari, M., Scarlato, P., 2020. The
901 role of undercooling during clinopyroxene growth in trachybasaltic magmas: Insights on magma
902 decompression and cooling at Mt. Etna volcano. *Geochim. Cosmochim. Acta* 268, 258–276.

903 Mollo, S., Del Gaudio, P., Ventura, G., Iezzi, G., Scarlato, P., 2010. Dependence of clinopyroxene
904 composition on cooling rate in basaltic magmas: implications for thermobarometry. *Lithos* 118, 302–
905 312.

906 Mollo, S., Misiti, V., Scarlato, P., Soligo, M., 2012. The role of cooling rate in the origin of high
907 temperature phases at the chilled margin of magmatic intrusions. *Chem. Geol.* 322–323, 28–46.

908 Mollo, S., Blundy, J.D., Iezzi, G., Scarlato, P., Langone, A., 2013. The partitioning of trace elements
909 between clinopyroxene and trachybasaltic melt during rapid cooling and crystal growth. *Contrib Mineral*
910 *Petrol* 166, 1633–1654.

911 Mollo, S., Masotta, M., 2014. Optimizing pre-eruptive temperature estimates in thermally and
912 chemically zoned magma chambers. *Chem. Geol.* 368, 97–103.

913 Mollo, S., Giacomoni, P.P., Andronico, D., Scarlato, P., 2015a. Clinopyroxene and titanomagnetite
914 cation redistributions at Mt. Etna volcano (Sicily, Italy): footprints of the final solidification history of
915 lava fountains and lava flows. *Chem. Geol.* 406, 45–54

916 Mollo, S., Giacomoni, P.P., Coltorti, M., Ferlito, C., Iezzi, G., Scarlato, P., 2015b. Reconstruction
917 of magmatic variables governing recent Etnean eruptions: constraints from mineral chemistry and P–T–
918 fO₂–H₂O conditions. *Lithos* 212–215, 311–320.

919 Mollo, S., Hammer, J.E., 2017. Dynamic crystallization in magmas. In: *EMU Notes in Mineralogy*.
920 16. pp. 373–418.

921 Mollo, S., Blundy, J., Scarlato, P., De Cristofaro, S.P., Tecchiato, V., Di Stefano, F., Vetere, F.,
922 Holtz, F., Bachmann, O., 2018. An integrated P–T–H₂O–lattice strain model to quantify the role of
923 clinopyroxene fractionation on REE+Y and HFSE patterns of mafic alkaline magmas: Application to
924 eruptions at Mt. Etna. *Earth Sci Rev* 185, 32–56.

925 Morgan, D.J., Jerram, D.A., 2006. On estimating crystal shape for crystal size distribution analysis.
926 *J. Volcanol. Geotherm. Res.* 154, 1–7.

927 Murru, M., Montuori, C., Wyss, M., Privitera, E., 1999. The locations of magma chambers at Mt.
928 Etna, Italy, mapped by b-values. *Geophys. Res. Lett.* 26, 2553–2556.

929 Nascimento, M.L.F., Ferreira, E.B., Zannotto, E.D., 2004. Kinetics and mechanisms of crystal growth
930 and diffusion in a glass-forming liquid. *J. Chem. Phys.* 121, 8924–8928.

931 Orlando, A., D’Orazio, M., Armienti, P., Borrini, D., 2008. Experimental determination of
932 plagioclase and clinopyroxene crystal growth rates in an anhydrous trachybasalt from Mt Etna (Italy).
933 *European Journal of Mineralogy* 20, 653–664.

934 Patanè, D., De Gori, P., Chiarabba, C., Bonaccorso, A., 2003. Magma Ascent and the Pressurization
935 of Mount Etna’s Volcanic System. *Science* 299, 2061–2063.

936 Perinelli, C., Mollo, S., Gaeta, M., De Cristofaro, S.P., Palladino, D.M., Armienti, P., Scarlato, P.,
937 Putirka, K.D., 2016. An improved clinopyroxene-based hygrometer for Etnean magmas and implications
938 for eruption triggering mechanisms. *Am. Mineral.* 101, 2774–2777.

939 Perinelli, C., Mollo, S., Gaeta, M., De Cristofaro, S.P., Palladino, D.M., Scarlato, P., 2018. Impulsive
940 supply of volatile-rich magmas in the shallow plumbing system of Mt. Etna Volcano. *Minerals* 8, 482.

941 Petrone, C.M., Bugatti, G., Braschi, E., Tommasini, S., 2016. Pre-eruptive magmatic processes re-
942 timed using a non-isothermal approach to magma chamber dynamics. *Nat Commun* 7.

943 Petrone, C.M., Braschi, E., Francalanci, L., Casalini, M., Tommasini, S., 2018. Rapid mixing and
944 short storage timescale in the magma dynamics of a steady-state volcano. *Earth Planet. Sci. Lett.* 492,
945 206–221.

946 Polacci, M., Arzilli, F., La Spina, G., Le Gall, N., Cai, B., Hartley, M.E., Di Genova, D., Vo, N.T.,
947 Nonni, S., Atwood, R.C., Llewellyn, E.W., Lee, P.D., Burton, M.R., 2018. Crystallisation in basaltic
948 magmas revealed via in situ 4D synchrotron X-ray microtomography. *Sci Rep* 8, 8377–8383.

949 Polacci, M., Andronico, D., de' Michieli Vitturi, M., Taddeucci, J., Cristaldi, A., 2019. Mechanisms
950 of Ash Generation at Basaltic Volcanoes: The Case of Mount Etna, Italy. *Front. Earth Sci.* 7.

951 Pontesilli, A., Masotta, M., Nazzari, M., Mollo, S., Armienti, P., Scarlato, P., Brenna, M., 2019.
952 Crystallization kinetics of clinopyroxene and titanomagnetite growing from a trachybasaltic melt: New
953 insights from isothermal time-series experiments. *Chem. Geol.* 510, 113–129.

954 Putirka, K., 2008. Thermometers and barometers for volcanic systems. *Rev. Mineral. Geochem.* 69,
955 61–120. <http://dx.doi.org/10.2138/rmg.2008.69.3>.

956 Ratkowsky, D.A., 1990. *Handbook of Non-linear Regression Models*. Marcel Decker Inc., New
957 York.

958 Rutherford, M.J., Hill, P.M., 1993. Magma ascent rates from amphibole breakdown: An
959 experimental study applied to the 1980-1986 Mount St. Helens eruptions. *J. Geophys. Res.* 98, 19667–
960 19685.

961 Rutherford, M.J., 2008. Magma Ascent Rates. *Rev Mineral Geochem* 69, 241–271.

962 Schanofski, M., Fanara, S., Schmidt, B.C., 2019. CO₂–H₂O solubility in K-rich phonolitic and
963 leucititic melts. *Contrib Mineral Petrol* 174.

964 Simakin, A.G., Salova T.P., Armienti P., 2003. Kinetics of clinopyroxene growth from a hydrous
965 hawaiite melt. *Geochemistry Int.* 41, 1275-1286.

966 Sunagawa, I., 1981. Characteristics of crystal growth in nature as seen from the morphology of
967 mineral crystals. *Bull. Mineral.* 104, 81–87.

968 Sunagawa, I., 2005. *Crystals: Growth, Morphology and Perfection*. Cambridge University Press,
969 Cambridge.

970 Toramaru, A., 1991. Model of nucleation and growth of crystals in cooling magmas. *Contr. Mineral.*
971 *and Petrol.* 108, 106–117.

972 Toramaru, A., Noguchi, S., Oyoshihara, S., Tsune, A., 2008. MND(microlite number density) water
973 exsolution rate meter. *J. Volcanol. Geotherm. Res.* 175, 156–167.

974 Ubide, T., Kamber, B.S., 2018. Volcanic crystals as time capsules of eruption history. *Nat Commun*
975 *9*.

976 Ubide, T., Mollo, S., Zhao, J., Nazzari, M., Scarlato, P., 2019a. Sector-zoned clinopyroxene as a
977 recorder of magma history, eruption triggers, and ascent rates. *Geochim. Cosmochim. Acta* 251, 265–
978 283.

979 Ubide, T., Caulfield, J., Brandt, C., Bussweiler, Y., Mollo, S., Di Stefano, F., Nazzari, M., Scarlato,
980 P., 2019b. Deep Magma Storage Revealed by Multi-Method Elemental Mapping of Clinopyroxene
981 Megacrysts at Stromboli Volcano. *Front. Earth Sci.* 7.

982 Vetere, F., Iezzi, G., Behrens, H., Holtz, F., Ventura, G., Misiti, V., Cavallo, A., Mollo, S., Dietrich,
983 M., 2015. Glass forming ability and crystallization behavior of sub-alkaline silicate melts. *Earth Sci Rev*
984 *150*, 25–44.

985 Webb, S.L., Dingwell, D.B., 1995. Viscoelasticity. *Rev. Mineral. Geochem.* 32, 95–119.

986 Weill, D.E., Hon, R., Navrotsky, A., 1980. The igneous system CaMgSi₂O₆-CaAl₂Si₂O₆-
987 NaAlSi₃O₆: variations on a classic theme by Bowen. In: Hargraves RB (ed) *Physics of magmatic*
988 *processes*. Princeton University Press, Princeton, pp 49-92

989 Welsch, B., Hammer, J., Baronnet, A., Jacob, S., Hellebrand, E., Sinton, J., 2016. Clinopyroxene in
990 postshield Haleakala ankaramite: 2. Texture, compositional zoning and supersaturation in the magma.
991 *Contrib. Mineral. Petrol.* 171, 6.

992 Yilmaz, S., Özkan, O.T., Günay, V., 1996. Crystallization kinetics of basalt glass. *Ceram. Int.* 22,
993 477–481.

994 Zhang, Y., Ni, H., Chen, Y., 2010. Diffusion data in silicate melts. *Rev. Mineral. Geochem.* 72, 311–
995 408.

996

997 **Figure captions**

998 Figure 1. Example of BSE (back-scattered electron) photomicrographs processed via NIH Image J
999 software and reduced to binary type images (i.e., black vs. white color) by grey level thresholding (i.e.,
1000 image segmentation; [Armienti, 2008](#)). A Matlab© code is also reported in [Supplementary Material 1](#) to
1001 perform image processing operations in conjunction with NIH Image J. The retrieved textural parameters

1002 are 1) the equal-area best-fit ellipses and lengths of major (L) and minor (W) axes, 2) the surface area per
1003 unit volume, and 3) the area fraction of a given population within a plane that is comparable to its volume
1004 fraction.

1005

1006 Figure 2. Selected BSE (back-scattered electron) photomicrographs representative of run products from
1007 *Experimental Set ISO*, *Experimental Set ΔP* , and *Experimental Set CR*.

1008

1009 Figure 3. Variation of clinopyroxene content (% area) as a function of experimental conditions. Data
1010 refer to *Experimental Set ISO* and *Experimental Set ΔP* (a), and *Experimental Set CR* (b).

1011

1012 Figure 4. Variation of 3D aspect ratio (S_v^P) as a function of experimental conditions. Data refer to
1013 *Experimental Set ISO* and *Experimental Set ΔP* (a), and *Experimental Set CR* (b).

1014

1015 Figure 5. Total alkali *versus* silica (a) and Di + Hd *versus* CaTs + CaTiTs (b) diagrams showing
1016 experimental glass and clinopyroxene compositions, respectively. Natural compositions from eruptions
1017 at Mt. Etna volcano are also displayed for comparison.

1018

1019 Figure 6. Variation of $\ln G_{max}$ as a function of experimental conditions. Data refer to *Experimental Set*
1020 *ISO* and *Experimental Set ΔP* (a), and *Experimental Set CR* (b). Values of G_{max} modeled through the
1021 thermodynamic expression of crystal growth (cf. [Armienti, 2008](#)) are also displayed for comparison.

1022

1023 Figure 7. Thermodynamic modeling of crystal growth kinetics for the transition between interface-
1024 controlled and diffusion-controlled growth regimes arising at ~ 33 °C. Modeled trends are depicted in
1025 green and blue for temperatures of 1050 and 1100 °C, respectively. In order to isolate the effect of ΔT ,
1026 modeled trends are also compared with values of G_{max} (green and blue diamonds for 1050 and 1100 °C,
1027 respectively) from decompression and cooling rate experiments conducted over similar relaxation times
1028 (i.e., in the order of minutes for *$\Delta Pf-1100-2H_2O$* , *$\Delta Pf-1100-5H_2O$* , *$\Delta Pf-1100-H_2O+CO_2$* , *$\Delta Pf-1050-$*
1029 *$2H_2O$* , *$\Delta Pf-1050-5H_2O$* , *$\Delta Pf-1050-H_2O+CO_2$* , *$CR-1050-0.25$* , *$CR-1050-0.5$*).

1030

1031 Figure 8. Regression plot of maximum growth rate (G_{max}) *versus* experimental time (t) on a logarithmic
1032 scale (a). Data from this study are compared with those from previous experimental works investigating

1033 basaltic and trachybasaltic compositions that ~~virtually~~ reproduce the overall intrinsic variability of Monte
1034 Maletto Formation. **Experiments** were performed at conditions comparable with those of magmas erupted
1035 at Mt. Etna volcano (i.e., $P = 0.1-1,000$ MPa, $T = 1,050-1,150$ °C, $H_2O = 0-4$ wt.%, $fO_2 = NNO+1.5-$
1036 $NNO+2$, $\Delta T = 75-233$ °C, and $CR = 0.001-100$ °C s⁻¹; Baker, 2008; Mollo et al., 2013; Pontesilli et al.,
1037 2019; Masotta et al., 2020). Probability density functions of regression coefficients β_0 (b) and β_1 (c)
1038 obtained from Monte Carlo simulations, as well model uncertainty associated with the estimate of t_{max}
1039 (d) are also displayed.

1040

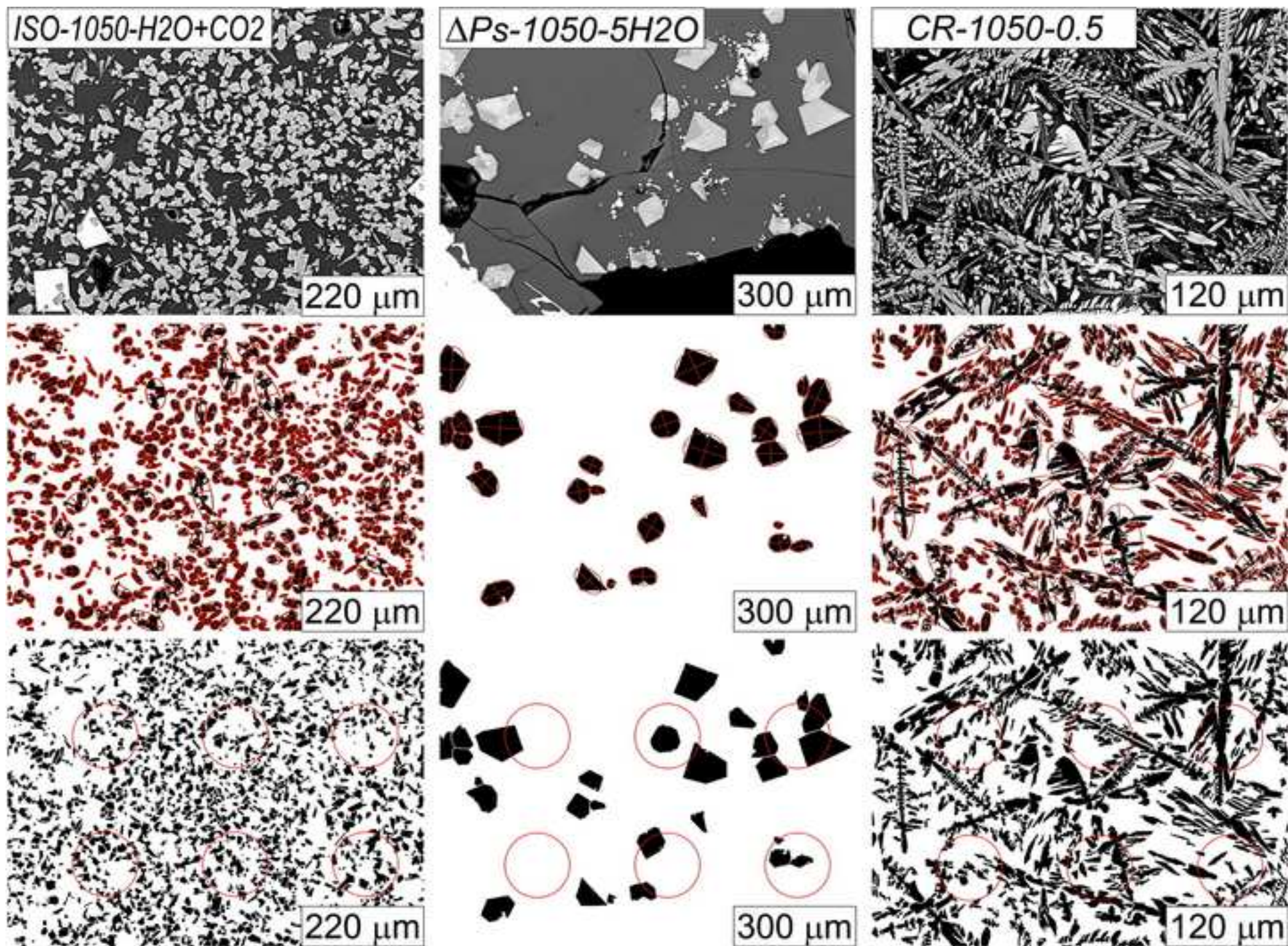
1041 Figure 9. Saturation conditions calculated for clinopyroxenes from 2011-2012 lava fountains erupted at
1042 Mt. Etna volcano. Uncorrected equilibrium between microphenocryst and bulk rock compositions has
1043 been determined for values of Kd_{Fe-Mg} (Fe-Mg exchange partition coefficient; Putirka, 2008), K_{Na} (Na
1044 partition coefficient; Blundy et al., 1995), and $DiHd$ (diopside + hedenbergite; Mollo et al., 2013). The
1045 equilibrium state of the bulk system has been corrected by minimizing the difference (Δ) between
1046 measured and predicted values. Using the model of Mollo et al. (2018), P - T - H_2O estimates have been
1047 adjusted within the calibration errors of the barometer (± 150 MPa), thermometer (± 20 °C), and
1048 hygrometer (± 0.45 wt.% H_2O), in order to minimize the overall uncertainty.

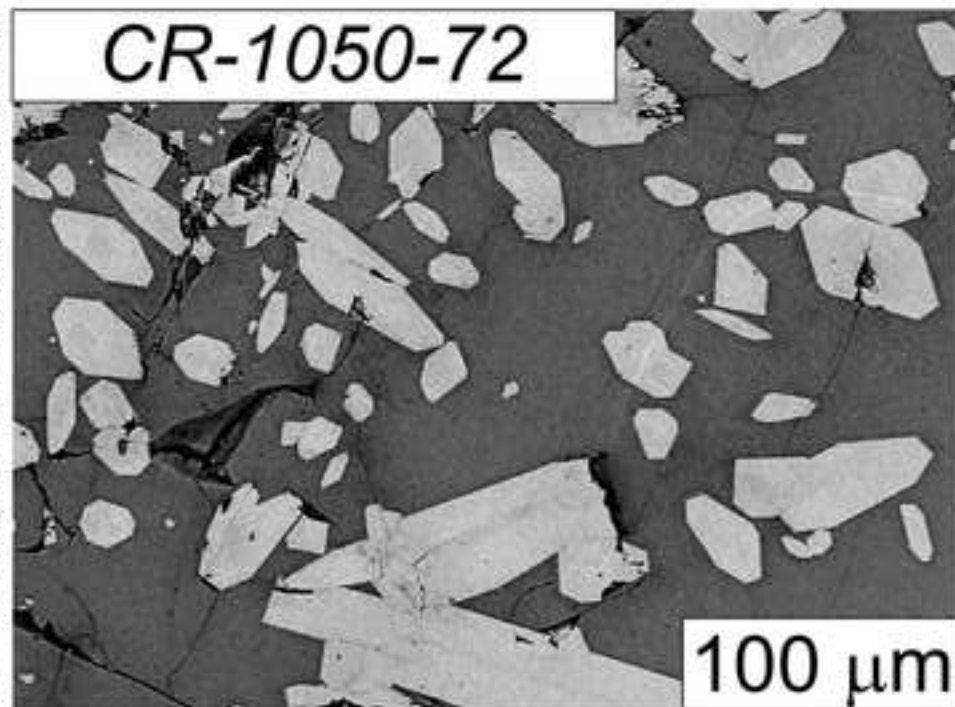
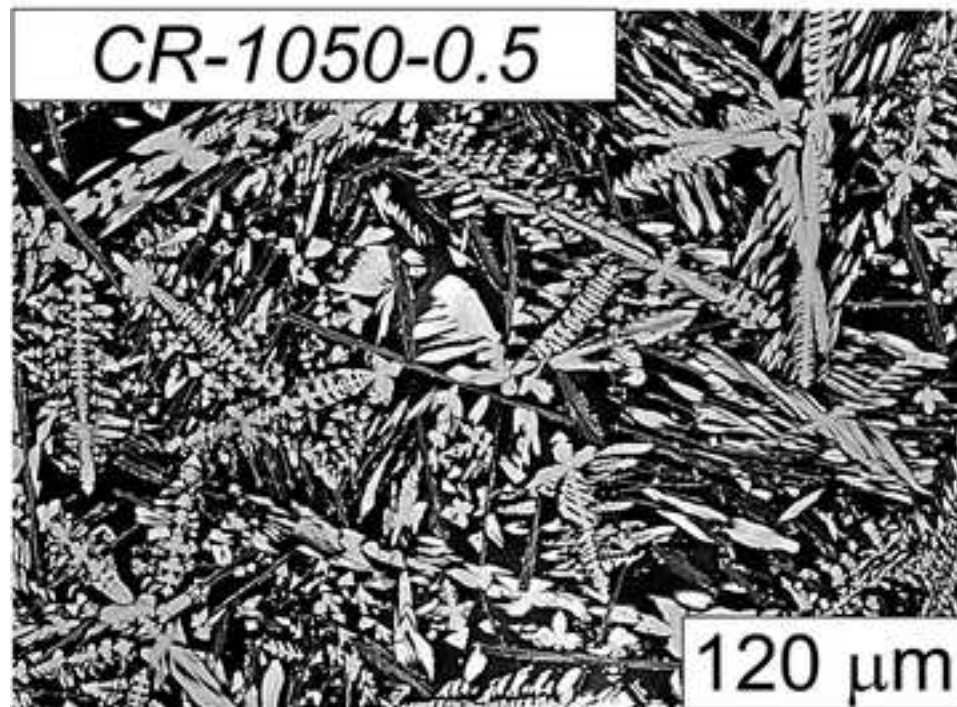
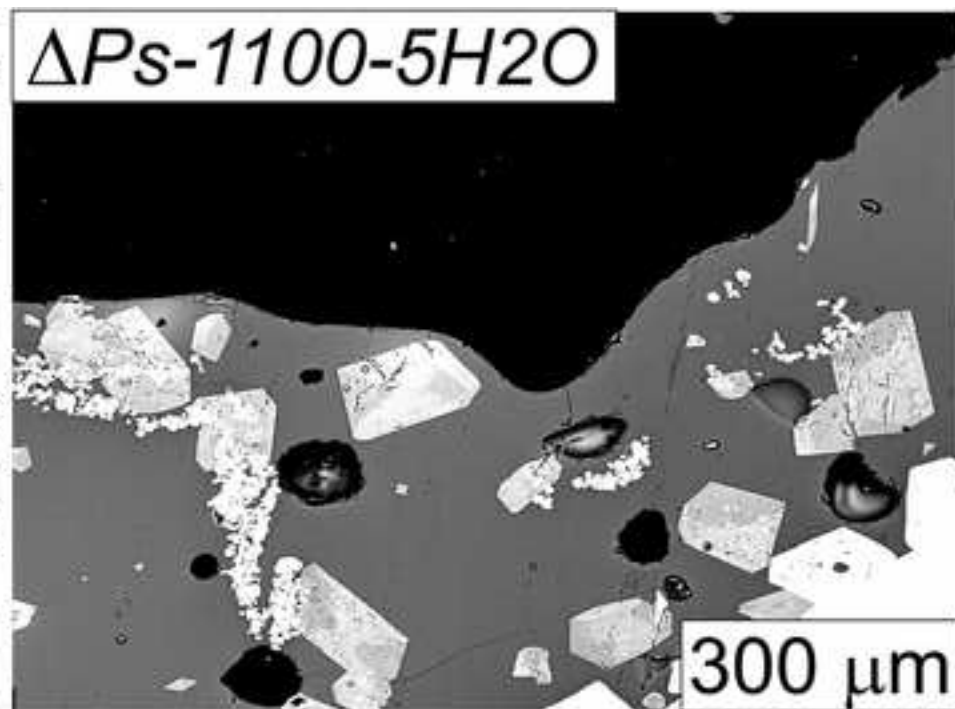
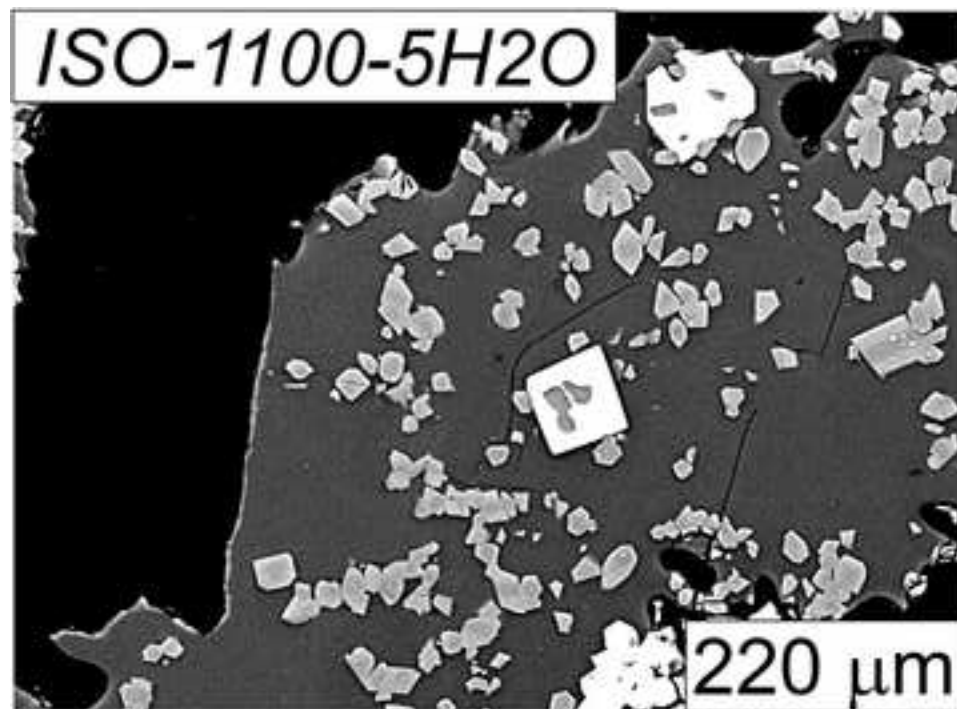
1049

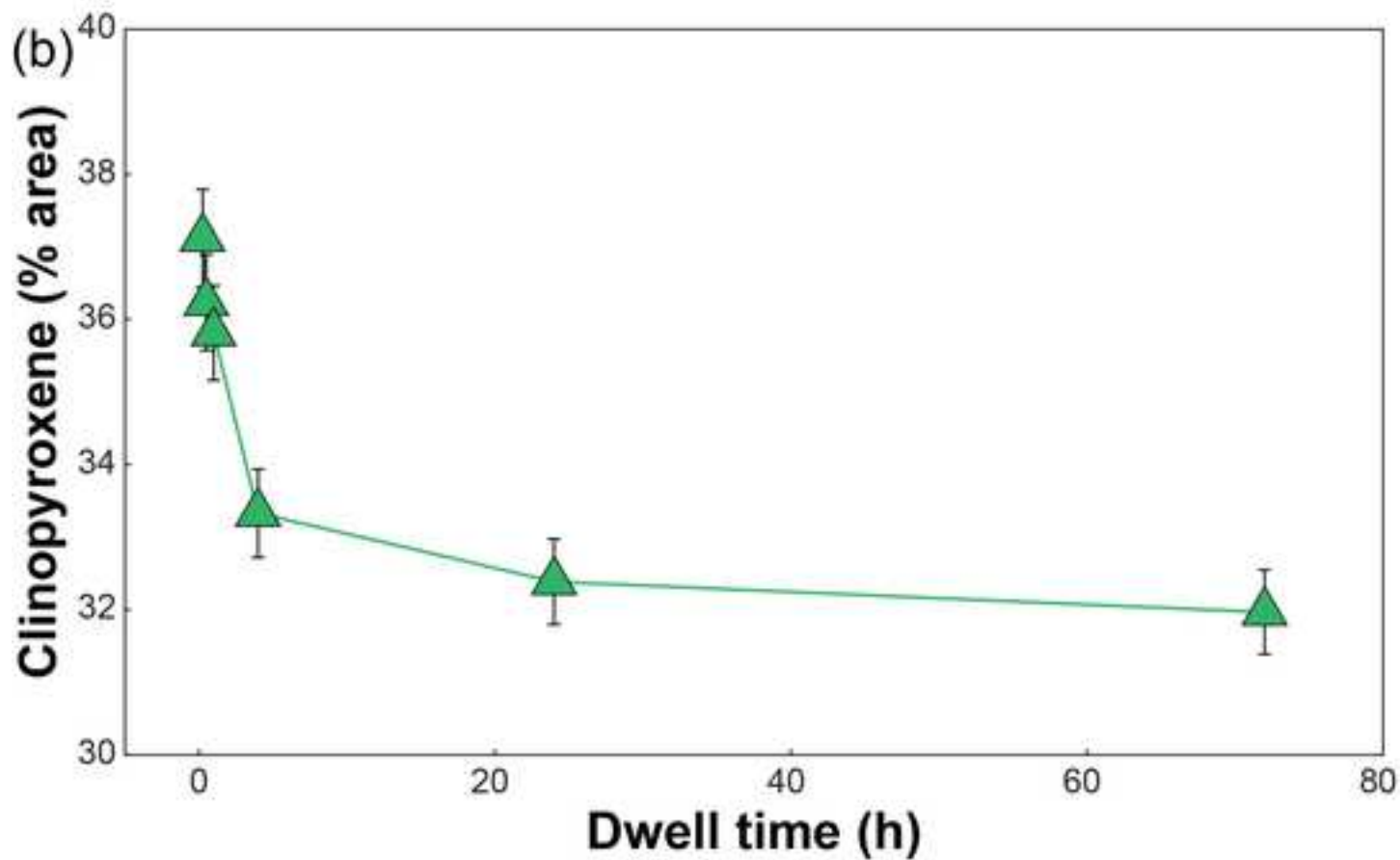
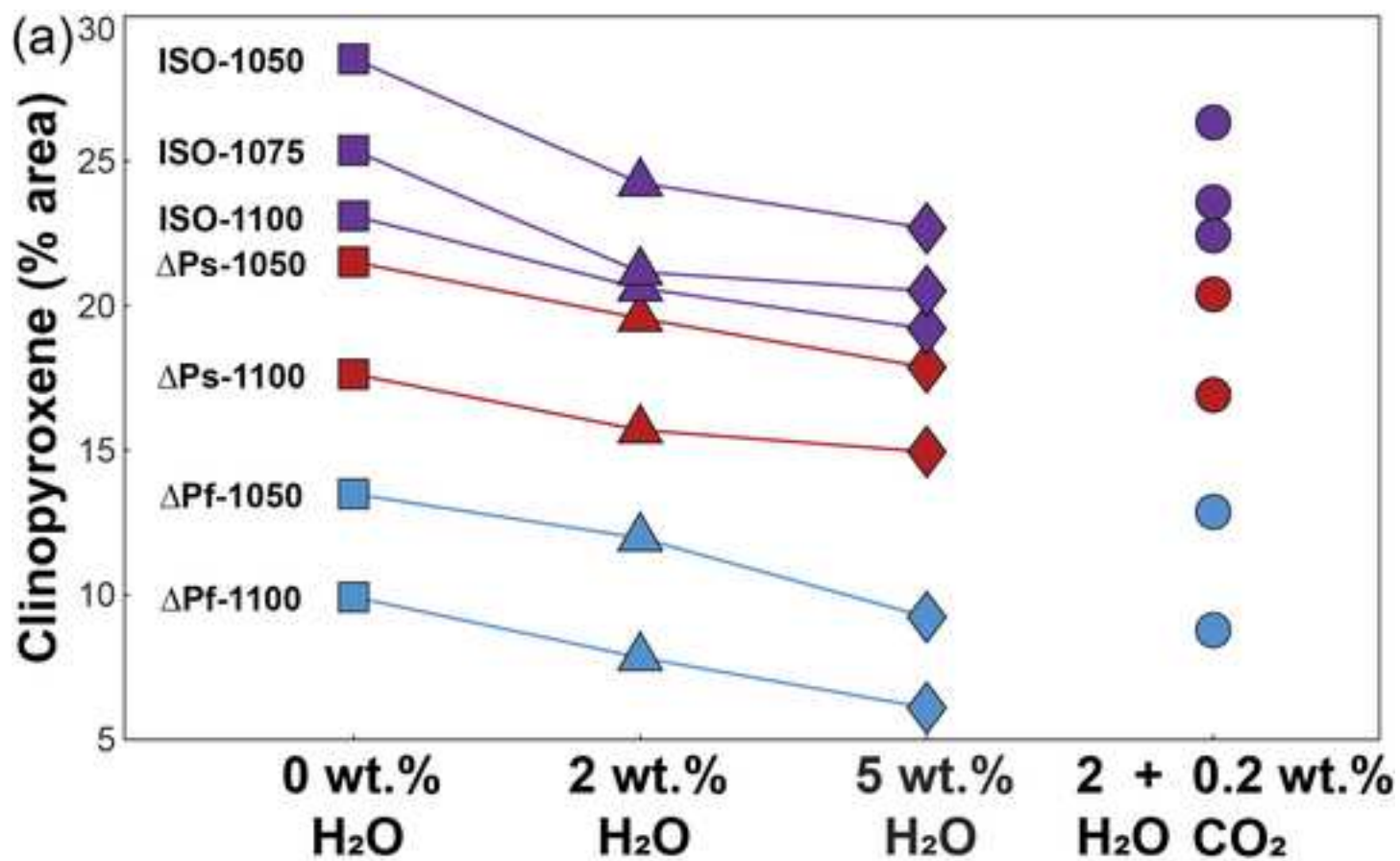
1050 Figure 10. Crystal size distribution (CSD) analysis of clinopyroxenes from 2011-2012 lava fountains
1051 erupted at Mt. Etna volcano. $N(L)$ versus L curves attest the occurrence of two distinct microphenocryst
1052 and microlite populations.

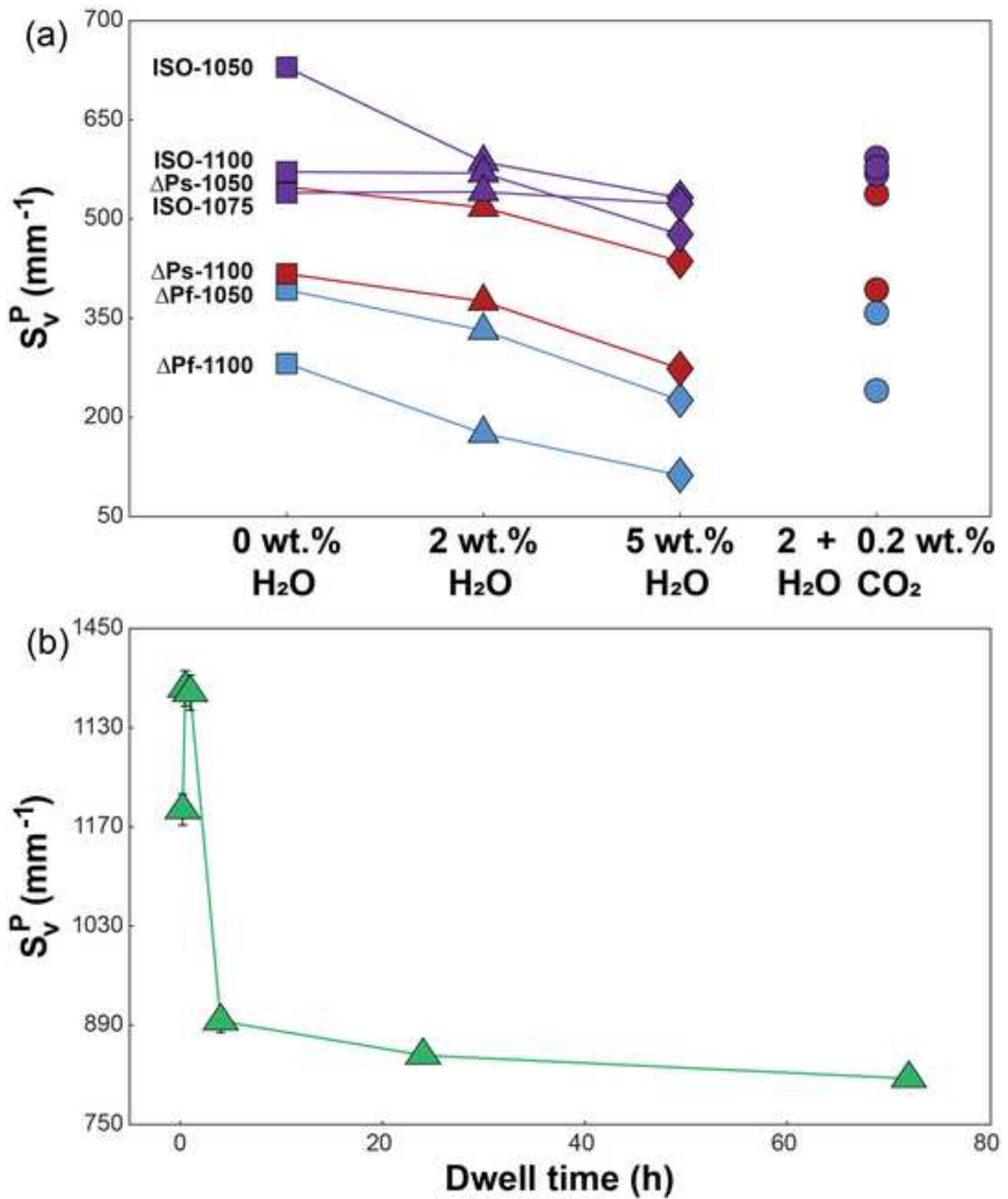
1053

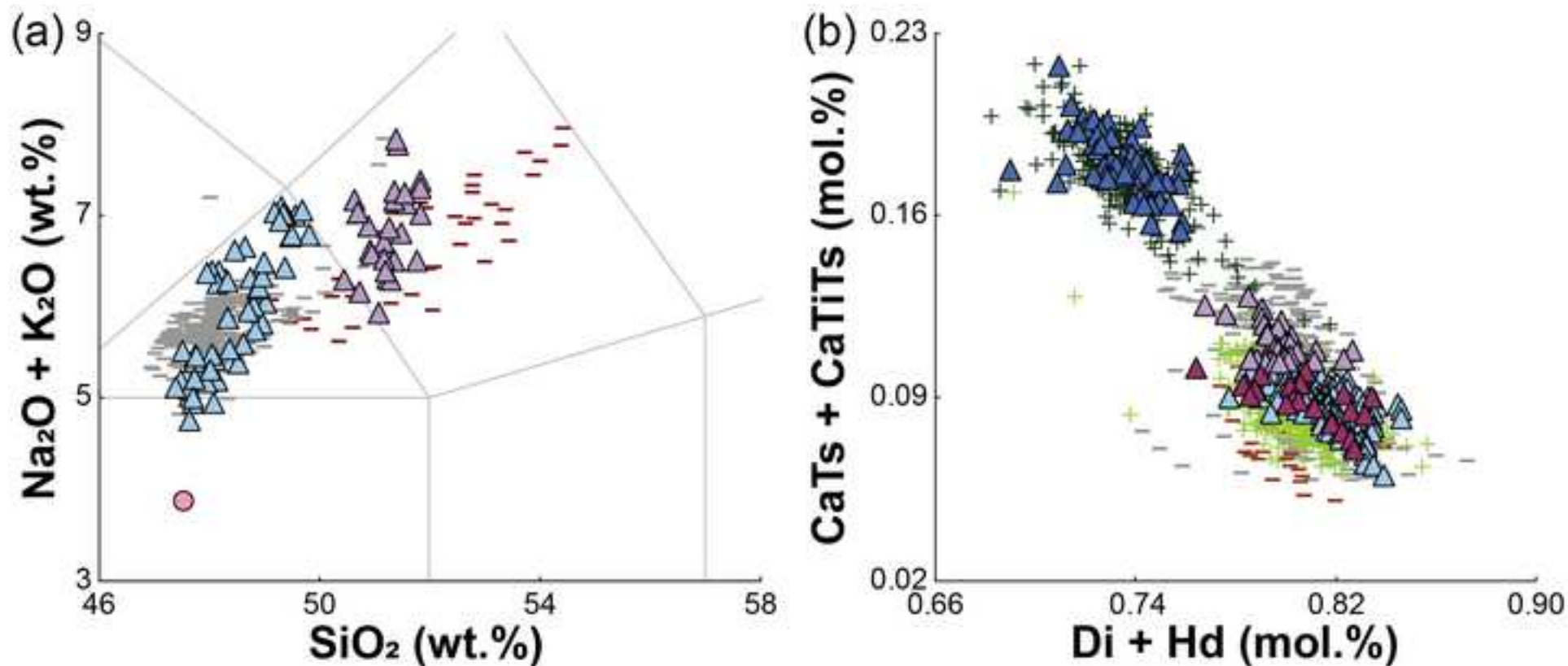
1054 Figure 11. Conceptual model of magma dynamics at Mt. Etna volcano describing the different time scales
1055 estimated for microlite and microphenocryst crystallization. Magma ascent velocities are also modeled
1056 accounting for either slow magma ascent rates within the interconnected storage regions forming the
1057 plumbing system architecture at depth or fast magma ascent rates within the uppermost part of the
1058 volcanic conduit and before eruption at the vent.



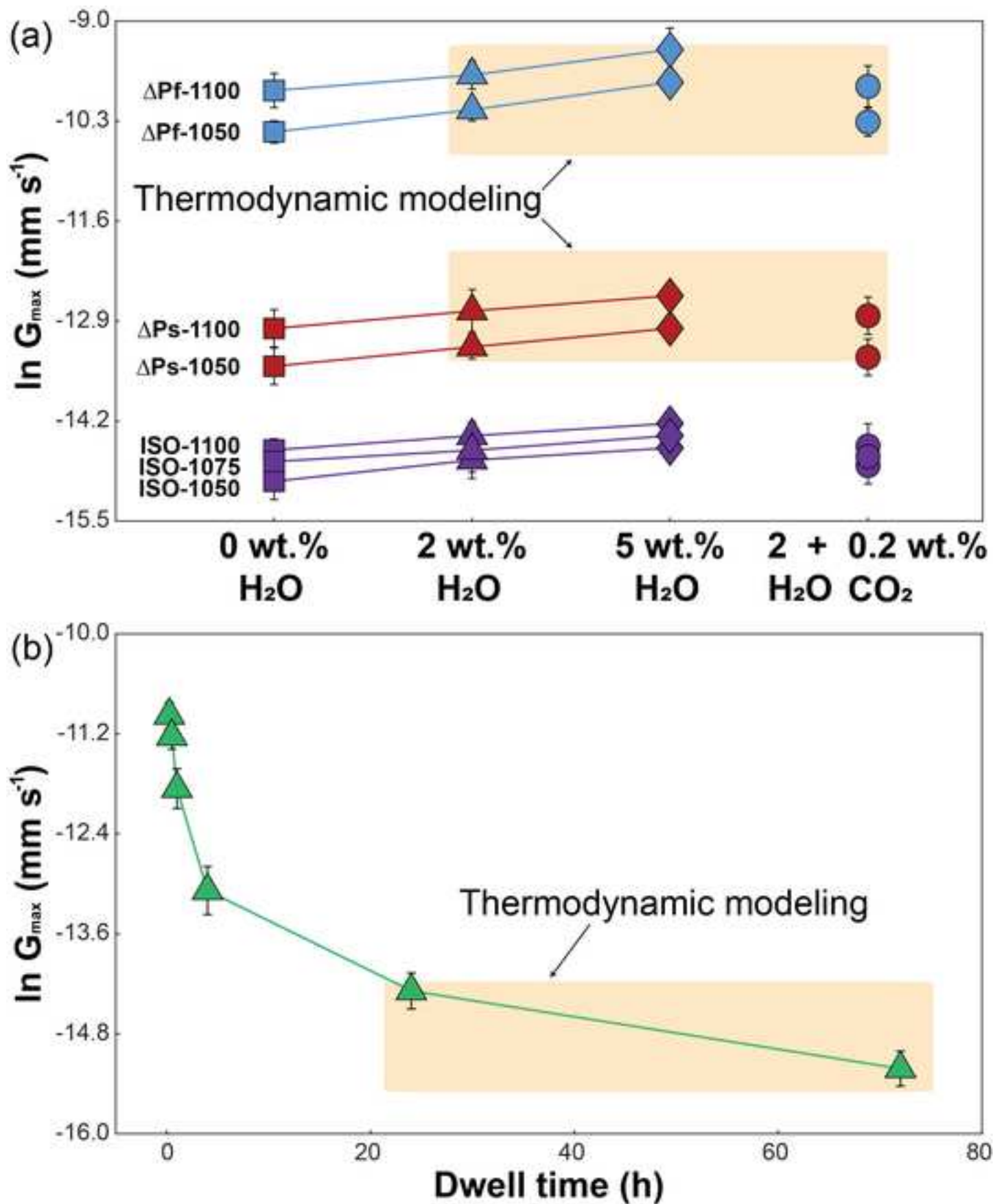


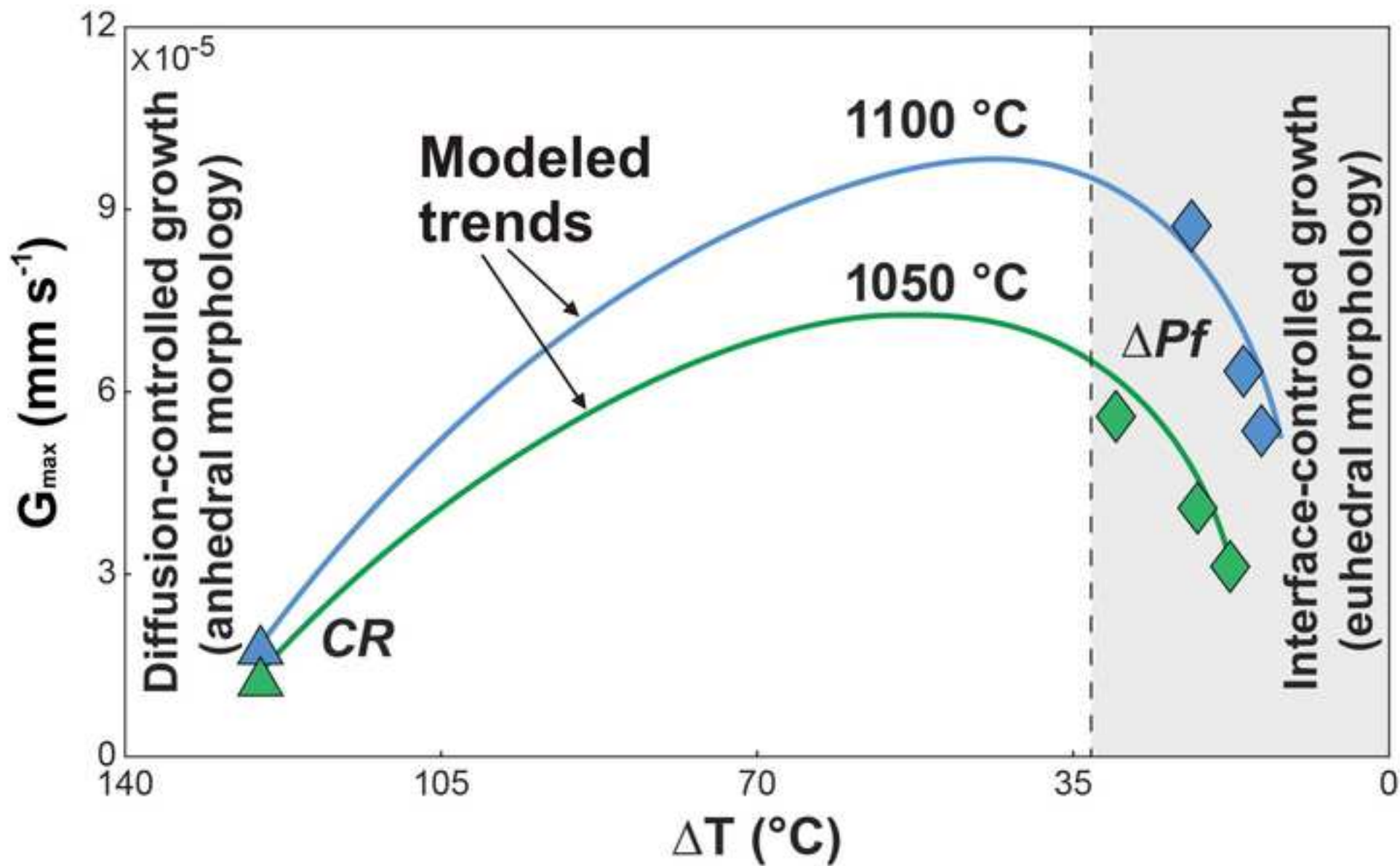


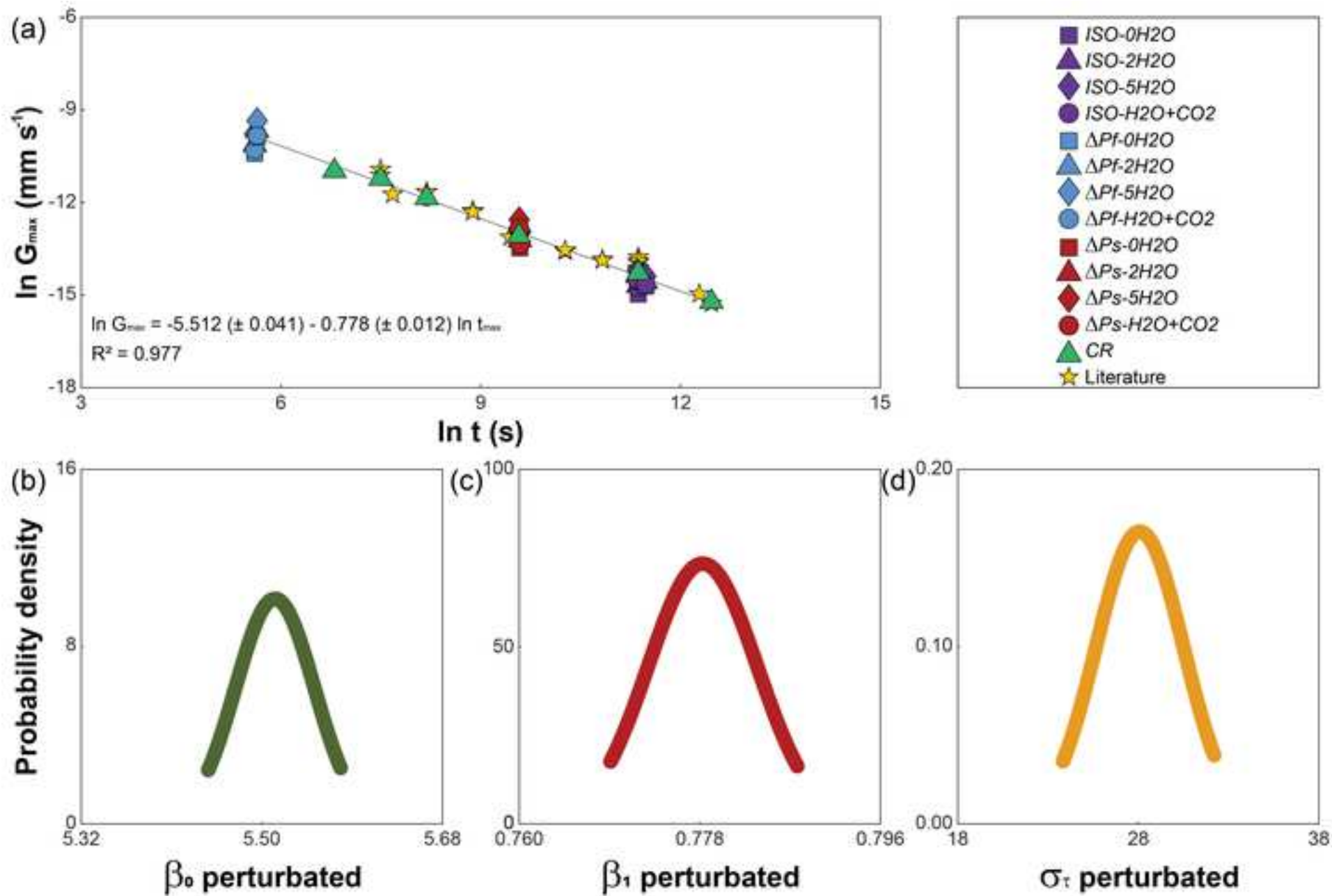


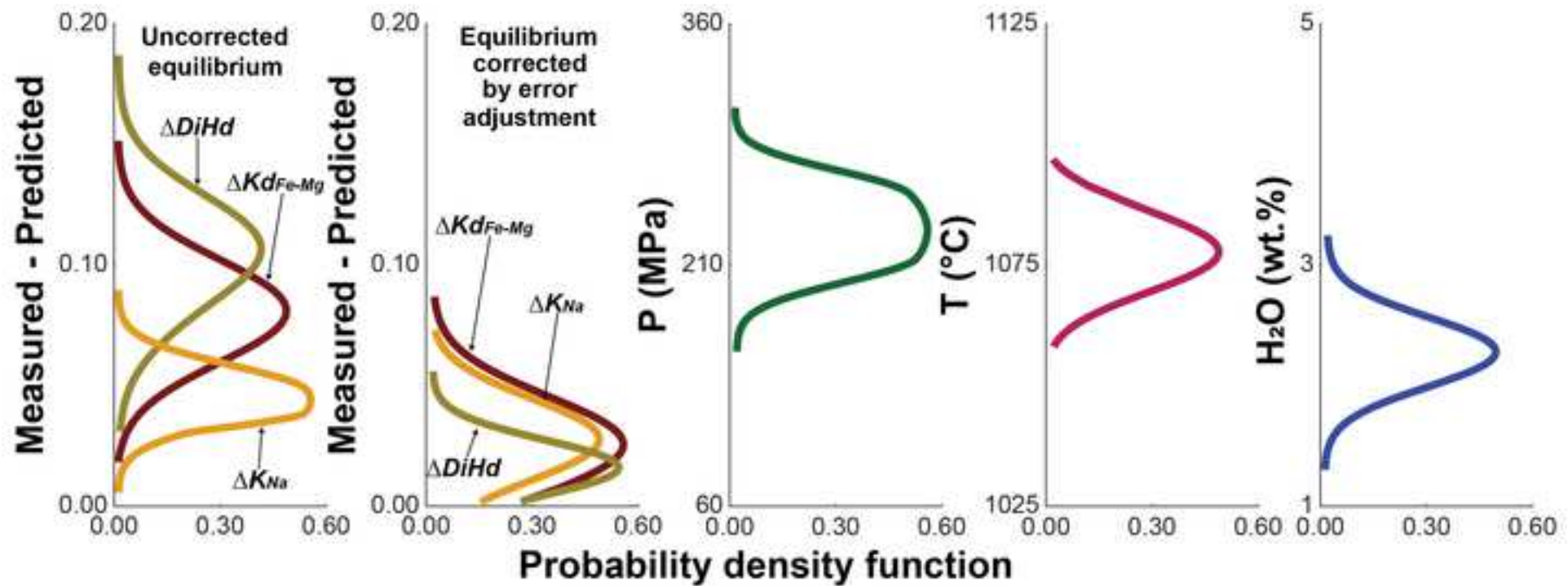


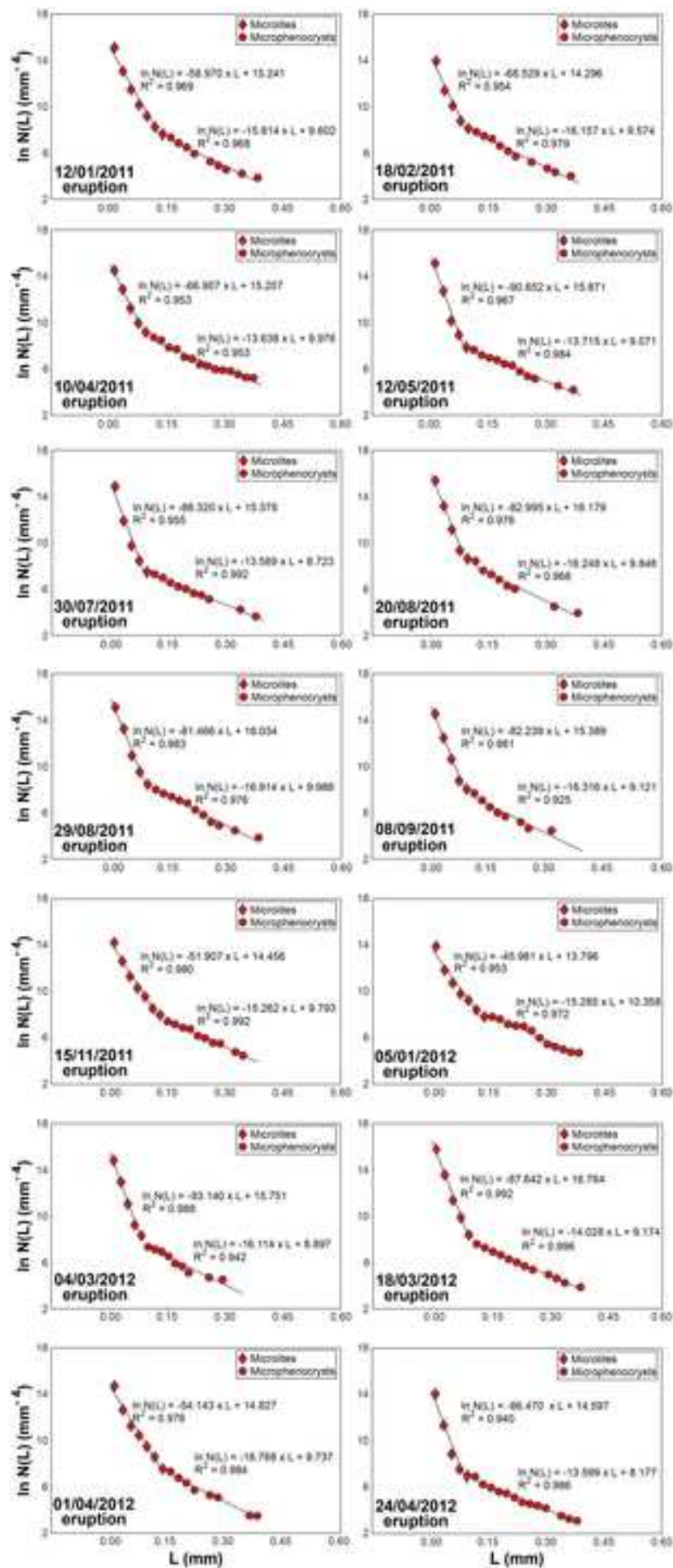
- Mt. Maletto
- Recent (post-1971) eruption
- Historic (pre-1971) eruption
- ▲ High-T, high- H_2O experiments (1100 °C and 5 wt.% H_2O)
- ▲ Low-T, low- H_2O experiments (1050-1075 °C and 0-2 wt.% H_2O)
- + Hourglass sectors $\{-1\ 1\ 1\}$ from recent (post-1971) eruptions
- + Prism sectors $\{1\ 0\ 0\}$ from recent (post-1971) eruptions
- ▲ Hourglass sectors $\{-1\ 1\ 1\}$ from decompression experiments
- ▲ Prism sectors $\{1\ 0\ 0\}$ from decompression experiments











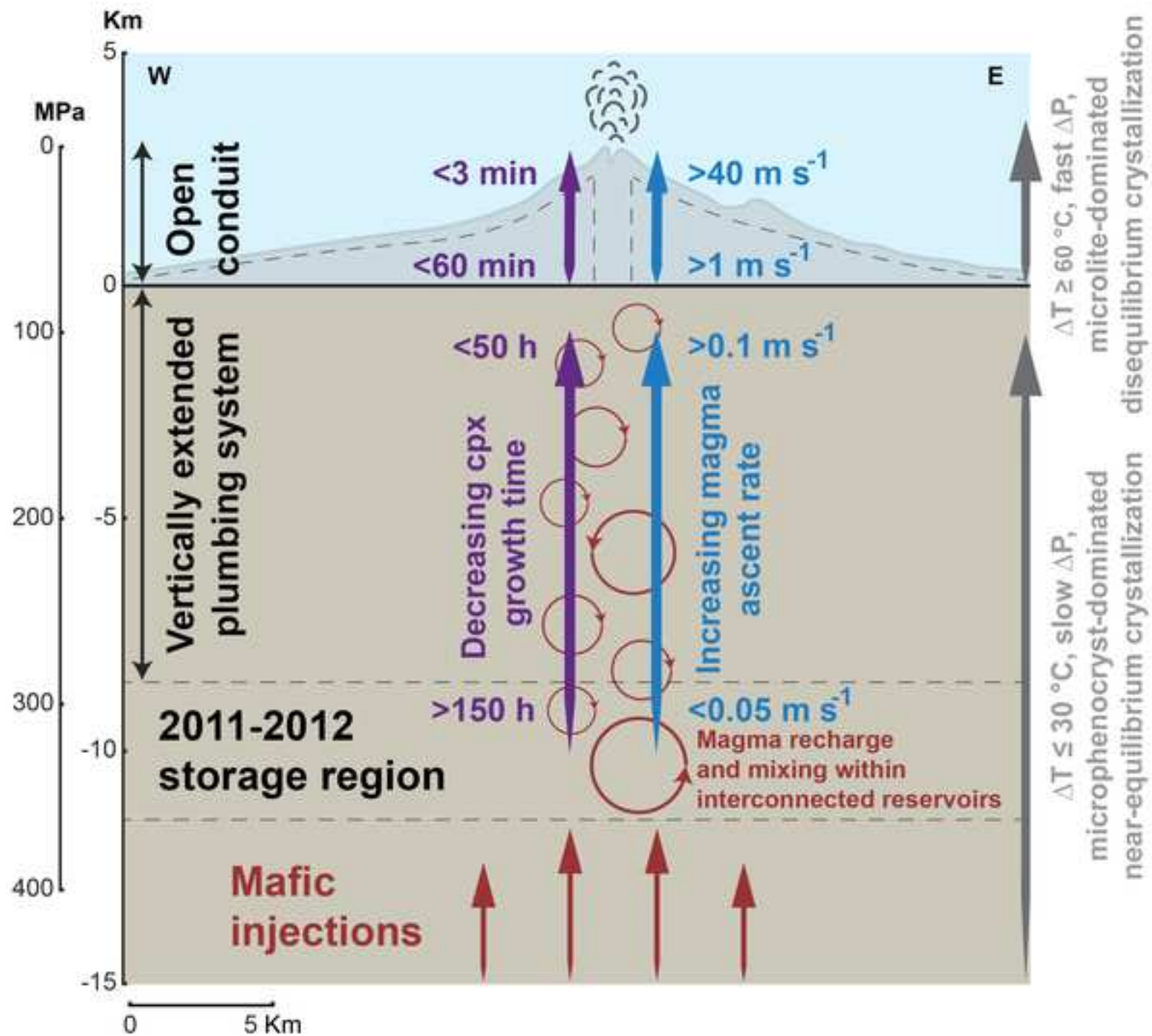



Table 1. Experimental conditions and clinopyroxene textural parameters.

	T (°C)	ΔT (°C)	H ₂ O (wt.%)	CO ₂ (wt.%)	t (h)	fO ₂ buffer	P _f (MPa)	ΔP (MPa s ⁻¹)	CR (°C min ⁻¹)	G _{max} × 10 ⁻⁸ (mm s ⁻¹)	Area %	S _v ^P (mm ⁻¹)
<i>Isothermal experiments - 300 MPa</i>												
ISO-1100-0H ₂ O	1100	-	0	-	23.70	NNO+2.1±0.2	-	-	-	46.88±7.1	22.82±0.43	571.43±10.42
ISO-1100-2H ₂ O	1100	-	2	-	23.70	NNO+2.1±0.2	-	-	-	56.45±4.96	20.23±0.38	569.3±10.38
ISO-1100-5H ₂ O	1100	-	5	-	23.70	NNO+2.1±0.2	-	-	-	66.25±3.84	18.77±0.35	476.81±8.7
ISO-1100-H ₂ O+CO ₂	1100	-	2	0.2	23.70	NNO+2.1±0.2	-	-	-	49.44±8.24	22.12±0.42	568.1±10.36
ISO-1075-0H ₂ O	1075	-	0	-	26.87	NNO+2.1±0.2	-	-	-	40.36±4.13	25.18±0.47	539.67±9.84
ISO-1075-2H ₂ O	1075	-	2	-	26.87	NNO+2.1±0.2	-	-	-	46.7±7.76	20.81±0.39	541.16±9.87
ISO-1075-5H ₂ O	1075	-	5	-	26.87	NNO+2.1±0.2	-	-	-	56.53±5.02	20.13±0.38	523.06±9.54
ISO-1075-H ₂ O+CO ₂	1075	-	2	0.2	26.87	NNO+2.1±0.2	-	-	-	43.14±4.41	23.32±0.44	577.96±10.54
ISO-1050-0H ₂ O	1050	-	0	-	24.00	NNO+2.1±0.2	-	-	-	31.17±3.68	28.47±0.54	729.64±13.31
ISO-1050-2H ₂ O	1050	-	2	-	24.00	NNO+2.1±0.2	-	-	-	41.09±4.85	24±0.45	586.28±10.69
ISO-1050-5H ₂ O	1050	-	5	-	24.00	NNO+2.1±0.2	-	-	-	48.19±1.94	22.38±0.42	532.11±9.71
ISO-1050-H ₂ O+CO ₂	1050	-	2	0.2	24.00	NNO+2.1±0.2	-	-	-	38.25±4.51	26.18±0.49	592.65±10.81
<i>Decompression experiments - 300 MPa</i>												
DPf-1100-0H ₂ O	1100	-	0	-	0.08	NNO+2.1±0.2	30	0.965	-	5092.01±565.09	9.12±0.16	281.59±5.13
DPf-1100-2H ₂ O	1100	16	2	-	0.08	NNO+2.1±0.2	30	0.965	-	6240.78±832.28	6.94±0.12	175.67±3.2
DPf-1100-5H ₂ O	1100	22	5	-	0.08	NNO+2.1±0.2	30	0.965	-	8677.78±1090.97	5.14±0.09	112.56±2.05
DPf-1100-H ₂ O+CO ₂	1100	14	2	0.2	0.08	NNO+2.1±0.2	30	0.965	-	5370.43±684.36	7.93±0.14	240.81±4.39
DPf-1050-0H ₂ O	1050	-	0	-	0.08	NNO+2.1±0.2	30	0.980	-	2970.19±225.2	12.83±0.23	392.86±7.16
DPf-1050-2H ₂ O	1050	20	2	-	0.08	NNO+2.1±0.2	30	0.980	-	3960.26±300.26	11.24±0.2	331.47±6.04
DPf-1050-5H ₂ O	1050	30	5	-	0.08	NNO+2.1±0.2	30	0.980	-	5673.47±558.95	8.4±0.15	226.13±4.12
DPf-1050-H ₂ O+CO ₂	1050	18	2	0.2	0.08	NNO+2.1±0.2	30	0.980	-	3377.53±307.94	12.18±0.22	358.13±6.53
DPs-1100-0H ₂ O	1100	-	0	-	4.01	NNO+2.1±0.2	30	0.019	-	228.86±26.83	17.13±0.31	417.19±7.61
DPs-1100-2H ₂ O	1100	16	2	-	4.01	NNO+2.1±0.2	30	0.019	-	287.4±38.34	15.12±0.27	375.47±6.85
DPs-1100-5H ₂ O	1100	22	5	-	4.01	NNO+2.1±0.2	30	0.019	-	350.34±24.56	14.34±0.26	273.84±4.99
DPs-1100-H ₂ O+CO ₂	1100	14	2	0.2	4.01	NNO+2.1±0.2	30	0.019	-	270.06±31.66	16.39±0.29	393.29±7.17
DPs-1050-0H ₂ O	1050	-	0	-	4.05	NNO+2.1±0.2	30	0.018	-	139.81±16.51	21.17±0.38	548.21±10
DPs-1050-2H ₂ O	1050	20	2	-	4.05	NNO+2.1±0.2	30	0.018	-	179.9±14.01	19.14±0.34	517.53±9.44
DPs-1050-5H ₂ O	1050	30	5	-	4.05	NNO+2.1±0.2	30	0.018	-	228.94±7.34	17.38±0.31	436.09±7.95
DPs-1050-H ₂ O+CO ₂	1050	18	2	0.2	4.05	NNO+2.1±0.2	30	0.018	-	157.29±18.57	20±0.36	537.89±9.81
<i>Cooling rate experiments - 300 MPa</i>												
CR-1050-0.25	1050	125	2	-	0.25	NNO+2	-	-	80	1706.11±134.49	37.11±0.67	1194.08±21.79
CR-1050-0.5	1050	125	2	-	0.5	NNO+2	-	-	80	1323.1±104.61	36.23±0.66	1365.44±24.91

<i>CR-1050-1</i>	1050	125	2	-	1	NNO+2	-	-	80	708.45±83.66	35.81±0.65	1359.31±24.8
<i>CR-1050-4</i>	1050	125	2	-	4	NNO+2	-	-	80	208.29±26.34	33.32±0.6	895.86±16.34
<i>CR-1050-24</i>	1050	125	2	-	24	NNO+2	-	-	80	62.53±6.47	32.38±0.59	847.57±2.74
<i>CR-1050-72</i>	1050	125	2	-	72	NNO+2	-	-	80	24.58±2.53	31.96±0.58	814.87±1.73

Table 2. Clinopyroxene length, CSD slope and intercept, maximum growth time and ascent rate of 2011-2012 lava fountains.

Eruption date	Clinopyroxene population	Crystal length (mm)	CSD slope (mm ⁻¹)	CSD intercept (mm ⁻⁴)	Maximum growth time (min)	error (±)	Maximum growth time (h)	error (±)	Ascent rate (m s ⁻¹) 1.5 km depth	error (±)	Ascent rate (m s ⁻¹) 10 km depth	error (±)
12/01/2011	Microlite	$L < 0.14$	-58.970	15.241	10.85	2.82	0.18	0.05	2.30	0.60	-	-
	Microphenocryst	$0.14 \leq L < 0.4$	-15.814	9.602	4122.86	1071.94	68.71	17.87	-	-	0.04	0.01
18/02/2011	Microlite	$L < 0.1$	-68.529	14.296	5.51	1.43	0.09	0.02	4.54	1.18	-	-
	Microphenocryst	$0.1 \leq L < 0.4$	-16.157	9.574	3742.32	973.00	62.37	16.22	-	-	0.04	0.01
10/04/2011	Microlite	$L < 0.1$	-66.907	15.207	6.14	1.60	0.10	0.03	4.07	1.06	-	-
	Microphenocryst	$0.1 \leq L < 0.4$	-13.638	9.976	8039.13	2090.17	133.99	34.84	-	-	0.02	0.01
12/05/2011	Microlite	$L < 0.1$	-90.652	15.871	1.56	0.41	0.03	0.01	16.04	4.17	-	-
	Microphenocryst	$0.1 \leq L < 0.4$	-13.715	9.071	7837.45	2037.74	130.62	33.96	-	-	0.02	0.01
30/07/2011	Microlite	$L < 0.1$	-88.320	15.378	1.75	0.46	0.03	0.01	14.26	3.71	-	-
	Microphenocryst	$0.1 \leq L < 0.4$	-13.589	8.723	8173.49	2125.11	136.22	35.42	-	-	0.02	0.01
20/08/2011	Microlite	$L < 0.1$	-82.995	16.179	2.32	0.60	0.04	0.01	10.77	2.80	-	-
	Microphenocryst	$0.1 \leq L < 0.4$	-16.248	9.848	3648.66	948.65	60.81	15.81	-	-	0.05	0.01
29/08/2011	Microlite	$L < 0.1$	-81.466	16.034	2.52	0.66	0.04	0.01	9.90	2.57	-	-
	Microphenocryst	$0.1 \leq L < 0.4$	-16.914	9.988	3043.65	791.35	50.73	13.19	-	-	0.05	0.01
08/09/2011	Microlite	$L < 0.1$	-82.239	15.389	2.42	0.63	0.04	0.01	10.34	2.69	-	-
	Microphenocryst	$0.1 \leq L < 0.4$	-16.316	9.121	3580.53	930.94	59.68	15.52	-	-	0.05	0.01
15/11/2011	Microlite	$L < 0.14$	-51.907	14.456	19.30	5.02	0.32	0.08	1.30	0.34	-	-
	Microphenocryst	$0.14 \leq L < 0.4$	-15.262	9.793	4839.92	1258.38	80.67	20.97	-	-	0.03	0.01
05/01/2012	Microlite	$L < 0.14$	-45.981	13.796	33.36	8.67	0.56	0.14	0.75	0.19	-	-
	Microphenocryst	$0.14 \leq L < 0.4$	-15.285	10.358	4807.14	1249.86	80.12	20.83	-	-	0.03	0.01
04/03/2012	Microlite	$L < 0.1$	-93.140	15.751	1.38	0.36	0.02	0.01	18.13	4.71	-	-
	Microphenocryst	$0.1 \leq L < 0.4$	-16.114	8.897	3787.60	984.78	63.13	16.41	-	-	0.04	0.01
18/03/2012	Microlite	$L < 0.1$	-87.642	16.764	1.82	0.47	0.03	0.01	13.77	3.58	-	-
	Microphenocryst	$0.1 \leq L < 0.4$	-14.028	9.174	7080.91	1841.04	118.02	30.68	-	-	0.02	0.01
01/04/2012	Microlite	$L < 0.14$	-54.143	14.827	15.96	4.15	0.27	0.07	1.57	0.41	-	-
	Microphenocryst	$0.14 \leq L < 0.4$	-16.768	9.737	3165.10	822.93	52.75	13.72	-	-	0.05	0.01
24/04/2012	Microlite	$L < 0.1$	-86.470	14.597	1.93	0.50	0.03	0.01	12.96	3.37	-	-
	Microphenocryst	$0.1 \leq L < 0.4$	-13.599	8.177	8146.40	2118.06	135.77	35.30	-	-	0.02	0.01



Click here to access/download

**Supplementary material/Appendix (Files for online
publication only)**

Original_binary_image.tif






Click here to access/download

**Supplementary material/Appendix (Files for online
publication only)**

Instruction(Moschini_et_al_2021.m).txt





Click here to access/download

**Supplementary material/Appendix (Files for online
publication only)**

Moschini_et_al_2021.m





Click here to access/download

**Supplementary material/Appendix (Files for online
publication only)**

Supplementary Material 2.xls



Click here to access/download

**Supplementary material/Appendix (Files for online
publication only)**

Supplementary Material 3.xls





Click here to access/download

**Supplementary material/Appendix (Files for online
publication only)**

Supplementary Material 4.xls

